Aalborg Universitet

AALBORG UNIVERSITY

DENMARK

Post-buckling optimization of composite structures using Koiter's method

Henrichsen, Søren Randrup; Weaver, Paul M.; Lindgaard, Esben; Lund, Erik

Post-buckling optimization of composite structures using Koiter's method

Søren R. Henrichsen[1*], Paul M. Weaver[2], Esben Lindgaard[1], and Erik Lund[1]

[1]*Department of Mechanical and Manufacturing Engineering, Aalborg University (AAU), Fibigerstræde 16, 9220 Aalborg East, Denmark*
[2]*Advanced Composites Centre for Innovation and Science, Department of Aerospace Engineering, University of Bristol, University Walk, Bristol, BS8 1TR, United Kingdom*

SUMMARY

Thin-walled structures, when compressed, are prone to buckling. To fully utilize the capabilities of such structures, the post-buckling response should be considered and optimized in the design process. This work presents a novel method for gradient based design optimization of the post-buckling performance of structures. The post-buckling analysis is based on Koiter's asymptotic method. To perform gradient based optimization, the design sensitivities of the Koiter factors are derived and new design optimization formulations based on the Koiter factors are presented. The proposed optimization formulations are demonstrated on a composite square plate and a curved panel where the post-buckling stability is optimized.

KEY WORDS: Asymptotic post-buckling; Composite structures; Composite optimization; Continuous fiber angle optimization; Koiter's method; Post-buckling optimization

1. INTRODUCTION

Thin-walled structures are often designed such that buckling does not occur during service. To ensure a structure does not buckle, the specified buckling load is often much greater than the design load. If a structure can be allowed to buckle during operation, thus operating in the post-buckling regime, it enables the possibility to design lighter and more efficient structures. To enable such an approach, the engineer must optimize the post-buckling response of the structure. Fiber reinforced polymers are ideally suited for such design tasks, as these materials allow a high degree of tailoring of the considered structure, and thus applied here for the post-buckling design optimization of structures.

When optimizing structures, robustness of the resulting structure is of major importance, as the imperfection sensitivity can increase during the optimization process [1]. One method is to collect these into an equivalent geometric imperfection and use that to evaluate the knock-down in performance. Refs. [2, 3] demonstrate robust design optimization by combining "worst" shape imperfection optimization and laminate optimization, thereby efficiently decreasing the imperfection sensitivity of laminated composite structures. A different approach is to handle all imperfections simultaneously by modeling the uncertainties using statistics, therefore quantifying the imperfections arising from material, geometry, load etc., and perform robust buckling optimization based on the uncertainties, see e.g., [4] for a review of different approaches. Many textbooks describe the coupling between imperfections, buckling load factor, and post-buckling

---

*Correspondence to: Department of Mechanical and Manufacturing Engineering, Aalborg University (AAU), Fibigerstræde 16, 9220 Aalborg East, Denmark. E-mail: srh@m-tech.aau.dk

stability, see e.g., [5]. Focusing on simple i.e., distinct buckling load factors, the sensitivity towards imperfections relates to the stability of the post-buckling response. Generally speaking, a stable post-buckled structure is less sensitive towards imperfections than an unstable post-buckled structure. Because of these considerations, the post-buckling stability can be utilized to design robust structures.

Post-buckling analysis of plates and shells has been subject to much research. Driven by the aerospace industry, large research projects have been concerned with the post-buckling response of stringer stiffened composite plate and shell structures. Refs. [6, 7, 8] present overviews and recommendations for analysis and design of stringer stiffened panels. These kinds of structures are used in the design of aerospace structures. Post-buckling analysis is computationally expensive, as it involves non-linearities. Often a path following algorithm like the arc-length method is used to trace the equilibrium curve [9, 10]. One powerful method to reduce the computational time is to apply asymptotic methods. In asymptotic methods the non-linear problem is substituted by a series of simpler problems, which are fast and easy to solve [11]. Furthermore, asymptotic methods extract the essential properties of the considered problem [11]. For bifurcation buckling, these properties relate to the type of buckling i.e., symmetric/asymmetric and the stability of the post-buckling response. In asymptotic methods the response is assumed to develop in a self-similar manner, and it cannot capture effects not included in the asymptotic expansion. Regardless, asymptotic methods have demonstrated applicability for post-buckling analysis of structures.

The early work in asymptotic post-buckling analysis was conducted by Koiter, who developed the so-called Koiter's method [12]. The method was developed to explain the large discrepancies between experiments and theoretical calculations observed in buckling of shell structures i.e., as a tool to evaluate the imperfection sensitivity of structures based on an approximation of the initial post-buckling response. Much research has been based on this method, and ref. [13] provides a comprehensive review of asymptotic post-buckling analysis. The analytical methods developed in [12] have been extended to multiple buckling modes and non-linear pre-buckling response, see e.g., [14, 15]. The demand for analyzing general structures led to the use of the Finite Element Method, and [16, 17, 18] have demonstrated Koiter's method using frame and shell elements. Koiter analysis with a geometrically non-linear pre-buckling response within a finite element framework has been demonstrated with co-rotational shell elements in [19], and shell elements based on a Total Lagrangian form in [20]. Recently, ref. [21] demonstrated Koiter analysis combined with the Differential Quadrature Method.

Koiter's method is only valid for a small post-buckling range. To extend the validity of the asymptotic approximation refs. [22, 23] developed the so-called Asymptotic Numerical Method (ANM). In ANM the Taylor like expansion from a Koiter analysis is post-processed by Padé approximants, thereby increasing the precision of the asymptotic approximation.

Design optimization using asymptotic methods is a relatively unexplored area. Analytical models combined with asymptotic expansions were implemented in the PANDA2 computer code and used to design minimum weight stiffened panels [24]. Ref. [25] applied Koiter's method to minimize the axial end shortening strain at a fixed load level for variable angle tow plates by optimizing first the lamination parameters and secondly search for a laminate with similar properties. Optimization of the post-buckling path tangent angle for constant and variable angle composite cylindrical shells is performed in [26] using genetic algorithms, where the potential of enhancing the post-buckling stability of structures is demonstrated. In this work we present a novel and generic method for post-buckling design optimization of laminated composite structures. The optimization is based on Koiter's method, which is used to extract the essential properties of the post-buckling response. Based on the information, we optimize the post-buckling stability of structures.

Continuous Fiber Angle Optimization (CFAO) is used for optimizing the post-buckling stability of the considered structures, so the fiber angles are used as design variables in this work. CFAO is known to result in non-convex design spaces with several local minima. Regardless, this parametrization is used as the laminate parametrization is not the focus of this work, and the equations are derived in a general sense, thus they can be used with different parametrizations like thickness variables, lamination parameters, Discrete Material Optimization etc.

The remainder of the paper is organized as follows: Section 2 presents different approaches for defining a post-buckling criteria and the approach selected in this work. In Section 3 the equations needed to conduct the asymptotic post-buckling analysis are presented. Section 4 presents the design sensitivity analysis for the asymptotic post-buckling response. The considered objective functions are presented in Section 5. Section 6 and Section 7 demonstrate the formulations through two examples which are a square plate and a curved panel. Lastly the findings are summed in Section 8.

2. POST-BUCKLING STABILITY CRITERIA

When considering the post-buckling response of standard structural elements such as beams, plates and shells, loaded in compression, two different displacement fields are of primary interest; the load-end shortening and the load-out-of-plane responses. A post-buckled design is not necessarily optimum for both responses, as demonstrated in [27, 28] for infinitely long, simply supported plates with symmetric and unsymmetric laminate layup and herein for finite dimension plates and panels without imposing constraints on the laminate layup. Consequently, it is important to determine which of the post-buckling responses is dominating the failure of the structure.

Defining post-buckling criteria based on the required inplane properties; compliance, end-shortening, end-strain etc., can be used if the failure of the structure is governed by in-plane properties. This has been demonstrated in e.g., [25] for buckling of plates. When optimizing the end shortening properties, the structure is allowed to buckle and the buckled shape is allowed to develop, but the effect of buckling on the inplane properties is minimized. Only the inplane response at the end load is considered, thus these objectives do not consider how the buckles develop. Consequently, a structure which does not possess any significant pre-buckling response can be designed. This is demonstrated in [29], where the effect of applying a compliance criterion for beams which exhibit snap-through behavior is shown. Here, the pre-buckling behavior of the structure is severely affected and a structure which exhibits snap-through buckling at a low load level is obtained.

The second approach is to minimize the out-of-plane effects in the post-buckling response. If e.g., a stringer stiffened panel is considered, skin-buckling does not cause gross failure of the panel. However, the buckled skin can induce a mode I crack opening between the skin and stringer and hence trigger skin-stiffener separation. This failure mechanism has been observed for a wind turbine blade, where failure of the blade was caused by skin buckling and subsequent delamination between the skin and main spar [30]. When minimizing the out-of-plane effects in the post-buckling response the development of the post-buckled shape is associated with as large an increase in load as possible.

The second approach followed in this work defines the post-buckling stability as the resistance towards development of buckles i.e., the more stable the structure the larger the load to cause a given out-of-plane deflection is required. The post-buckling response is obtained using Koiter's asymptotic analysis. Here the post-buckling stability is determined by the Koiter factors, in the remainder also called the Koiter a- and b-factors or simply the a- and b-factors. These factors give the change in the load factor in the post-buckling regime. The Koiter factors are global factors for the structure and not related to the response of a single degree of freedom. Defining a global factor ensures that the overall performance of the structure is optimized, and that change in the buckling mode shape can be accounted for during the optimization.

3. ASYMPTOTIC POST-BUCKLING ANALYSIS

The equations needed in order to conduct the asymptotic post-buckling analysis are conveniently derived using the Budiansky-Hutchinson notation. If the reader is not familiar with the Budiansky-Hutchinson notation, we refer to e.g., [14, 31]. The strain is defined using a set of l operators relating the displacements to the strains, providing a compact notation throughout the derivation, and noting that the symbols have different properties depending on the applied theory, e.g., beam, plate, or shell theory. In this work we focus on the continuum version. The non-linear strain relation represented

in the Budiansky-Hutchinson notation is given by

$$\boldsymbol{\epsilon} = l_1 \left(\boldsymbol{u} \right) + \frac{1}{2} l_2 \left(\boldsymbol{u} \right) \tag{1}$$

Here $\boldsymbol{\epsilon}$ are the strains, $\boldsymbol{u}$ is the displacement field, l_1 contains the linear part of the strains, and l_2 the non-linear part of the strains. In index notation, Equation (1) is equivalent to

$$\epsilon_{ij} = \underbrace{\frac{1}{2} \left(u_{i,j} + u_{j,i} \right)}_{l_1(\boldsymbol{u})} + \frac{1}{2} \underbrace{\left(u_{k,i} u_{k,j} \right)}_{l_2(\boldsymbol{u})}$$

When clarification is necessary, we switch to index notation, and the tensors have the same definition as the corresponding Budiansky-Hutchinson quantity. During the derivation a bilinear operator l_{11} is needed, and it is given by

$$\begin{aligned} l_2 \left(\boldsymbol{u} + \boldsymbol{v} \right) &= l_2 \left(\boldsymbol{u} \right) + 2 l_{11} \left(\boldsymbol{u}, \boldsymbol{v} \right) + l_2 \left(\boldsymbol{v} \right) \\ l_{11} \left(\boldsymbol{u}, \boldsymbol{v} \right) &= \frac{1}{2} \left(u_{k,i} v_{k,j} + u_{k,j} v_{k,i} \right) \end{aligned} \tag{2}$$

Here $\boldsymbol{u}$ and $\boldsymbol{v}$ represent two different displacement fields. The l_{11} operator is used when varying the total potential energy

$$\delta \boldsymbol{\epsilon} = l_1 \left(\delta \boldsymbol{u} \right) + l_{11} \left(\boldsymbol{u}, \delta \boldsymbol{u} \right) \tag{3}$$

3.1. Theory

To perform the asymptotic analysis we assume that a critical bifurcation point has been determined, and that the displacements and the load factor can be expanded into the post-buckling regime using a Taylor-like representation

$$\lambda = \lambda_c + a \lambda_c \xi + b \lambda_c \xi^2 + c \lambda_c \xi^3 + \dots \tag{4}$$

$$\boldsymbol{u} = {}^0\boldsymbol{u}(\lambda) + {}^1\boldsymbol{u}\xi + {}^c\boldsymbol{u} = {}^0\boldsymbol{u}(\lambda) + {}^1\boldsymbol{u}\xi + {}^2\boldsymbol{u}\xi^2 + {}^3\boldsymbol{u}\xi^3 + \dots \tag{5}$$

$$\boldsymbol{\epsilon} = {}^0\boldsymbol{\epsilon}(\lambda) + {}^1\boldsymbol{\epsilon}\xi + {}^2\boldsymbol{\epsilon}\xi^2 + {}^3\boldsymbol{\epsilon}\xi^3 + \dots \tag{6}$$

$$\boldsymbol{\sigma} = {}^0\boldsymbol{\sigma}(\lambda) + {}^1\boldsymbol{\sigma}\xi + {}^2\boldsymbol{\sigma}\xi^2 + {}^3\boldsymbol{\sigma}\xi^3 + \dots \tag{7}$$

Here λ is the post-buckling load factor normalized with respect to the applied load, λ_c is the critical buckling load factor, a, b, and c are the first three Koiter factors which are non-dimensional, ${}^0\boldsymbol{u}$ is the pre-buckling displacement field, ${}^1\boldsymbol{u}$ through ${}^3\boldsymbol{u}$ are the post-buckling displacement fields, and ξ is the perturbation variable. ${}^{0\dots3}\boldsymbol{\epsilon}$ and ${}^{0\dots3}\boldsymbol{\sigma}$ are the expanded strains and stresses with ^{0} being the pre-buckling quantities. The expansions for λ, $\boldsymbol{u}$, $\boldsymbol{\epsilon}$, and $\boldsymbol{\sigma}$ are assumed to be valid asymptotically as $\xi \to 0$. From Equation (4) some important properties of the post-buckling load factor can be determined. The initial post-buckling load factor is dominated by the $a\lambda_c$ part, since $|\xi^n| \ll |\xi|$ for $n \geq 2$. If $a\lambda_c$ is non-zero then the initial post-buckling response is unstable, since ξ can assume both positive and negative values. On the other hand, if $a\lambda_c \ll |\xi|$ for small $|\xi|$ then the initial post-buckling response is dominated by the $b\lambda_c$ factor, and the stability of the system is governed by the sign of the b-factor. A graphical interpretation is that the a-factor is the slope of the post-buckling path and the b-factor is the curvature of the path in a $\xi - \lambda$ plot. The post-buckling displacement field is represented by the ${}^1\boldsymbol{u}$ displacement field and a correction displacement field, ${}^c\boldsymbol{u}$, which is orthogonal to ${}^1\boldsymbol{u}$. ${}^c\boldsymbol{u}$ is represented by the post-buckling displacement fields ${}^2\boldsymbol{u}$, ${}^3\boldsymbol{u}$, $\dots$ which are orthogonal to ${}^1\boldsymbol{u}$, but not necessarily mutually orthogonal. The expanded strains are obtained by

differentiating the expanded displacements as

$$
\begin{aligned}
\epsilon_{ij} =& \frac{1}{2}\left({}^0u_{i,j}(\lambda) + {}^0u_{j,i}(\lambda) + {}^0u_{k,i}(\lambda){}^0u_{k,j}(\lambda)\right) + \frac{1}{2}\left({}^1u_{i,j} + {}^1u_{j,i} + {}^1u_{k,i}{}^1u_{k,j}\xi\right)\xi \\
&+ \frac{1}{2}\left({}^2u_{i,j} + {}^2u_{j,i} + {}^2u_{k,i}{}^2u_{k,j}\xi^2\right)\xi^2 + \frac{1}{2}\left({}^3u_{i,j} + {}^3u_{j,i} + {}^3u_{k,i}{}^3u_{k,j}\xi^3\right)\xi^3 \\
&+ \frac{1}{2}\left({}^0u_{k,i}(\lambda){}^1u_{k,j} + {}^0u_{k,j}(\lambda){}^1u_{k,i}\right)\xi + \frac{1}{2}\left({}^0u_{k,i}(\lambda){}^2u_{k,j} + {}^0u_{k,j}(\lambda){}^2u_{k,i}\right)\xi^2 \\
&+ \frac{1}{2}\left({}^0u_{k,i}(\lambda){}^3u_{k,j} + {}^0u_{k,j}(\lambda){}^3u_{k,i} + {}^1u_{k,i}{}^2u_{k,j} + {}^1u_{k,j}{}^2u_{k,i}\right)\xi^3 + \dots \quad (8) \\
=& \frac{1}{2}\left({}^0u_{i,j}(\lambda) + {}^0u_{j,i}(\lambda) + {}^0u_{k,i}(\lambda){}^0u_{k,j}(\lambda)\right) \\
&+ \frac{1}{2}\left({}^1u_{i,j} + {}^1u_{j,i} + {}^0u_{k,i}(\lambda){}^1u_{k,j} + {}^0u_{k,j}(\lambda){}^1u_{k,i}\right)\xi \\
&+ \frac{1}{2}\left({}^2u_{i,j} + {}^2u_{j,i} + {}^1u_{k,i}{}^1u_{k,j} + {}^0u_{k,i}(\lambda){}^2u_{k,j} + {}^0u_{k,j}(\lambda){}^2u_{k,i}\right)\xi^2 \\
&+ \frac{1}{2}\left({}^3u_{i,j} + {}^3u_{j,i} + {}^0u_{k,i}(\lambda){}^3u_{k,j} + {}^0u_{k,j}(\lambda){}^3u_{k,i} + {}^1u_{k,i}{}^2u_{k,j} + {}^1u_{k,j}{}^2u_{k,i}\right)\xi^3 + \dots \quad (9)
\end{aligned}
$$

and is equivalent to

$$
\begin{aligned}
\boldsymbol{\epsilon} =& l_1\left({}^0\boldsymbol{u}(\lambda)\right) + \frac{1}{2}l_2\left({}^0\boldsymbol{u}(\lambda)\right) + \left(l_1\left({}^1\boldsymbol{u}\right) + l_{11}\left({}^0\boldsymbol{u}(\lambda), {}^1\boldsymbol{u}\right)\right)\xi + \left(l_1\left({}^2\boldsymbol{u}\right) + \frac{1}{2}l_2\left({}^1\boldsymbol{u}\right)\right)\xi^2 \\
&+ l_{11}\left({}^0\boldsymbol{u}(\lambda), {}^2\boldsymbol{u}\right)\xi^2 + \left(l_1\left({}^3\boldsymbol{u}\right) + l_{11}\left({}^0\boldsymbol{u}(\lambda), {}^3\boldsymbol{u}\right) + l_{11}\left({}^1\boldsymbol{u}, {}^2\boldsymbol{u}\right)\right)\xi^3 + \dots \quad (10)
\end{aligned}
$$

By assuming linear pre-buckling ${}^0\boldsymbol{u}(\lambda) \equiv \lambda{}^0\boldsymbol{u}$ and ${}^0\boldsymbol{\epsilon}(\lambda) \equiv \lambda{}^0\boldsymbol{\epsilon}$. Linear pre-buckling implies that $l_2\left({}^0\boldsymbol{u}\right) = 0$ because the operator contains the non-linear part of the strain. Additionally, $l_{11}\left({}^0\boldsymbol{u}, \boldsymbol{v}\right) = 0$ for any displacement field $\boldsymbol{v}$, because the pre-buckling strains are small, and any product with these strains is much smaller than the remaining terms. From this, we can reduce Equation (10) to

$$
\boldsymbol{\epsilon} = \lambda\underbrace{l_1\left({}^0\boldsymbol{u}\right)}_{{}^0\boldsymbol{\epsilon}} + \underbrace{l_1\left({}^1\boldsymbol{u}\right)}_{{}^1\boldsymbol{\epsilon}}\xi + \underbrace{\left(l_1\left({}^2\boldsymbol{u}\right) + \frac{1}{2}l_2\left({}^1\boldsymbol{u}\right)\right)}_{{}^2\boldsymbol{\epsilon}}\xi^2 + \underbrace{\left(l_1\left({}^3\boldsymbol{u}\right) + l_{11}\left({}^1\boldsymbol{u}, {}^2\boldsymbol{u}\right)\right)}_{{}^3\boldsymbol{\epsilon}}\xi^3 + \dots \quad (11)
$$

The strains are coupled to the stresses by a linear constitutive operator, H, given by Equation (12).

$$
\boldsymbol{\sigma} = H\left(\boldsymbol{\epsilon}\right) \quad (12)
$$

From this the stresses have the same form as the strains in Equation (11).

The principle of virtual displacements is used to derive the equations needed for the asymptotic analysis. In tensor form the variational form of the total elastic potential is given by [31]

$$
\begin{aligned}
\delta\Pi(u_i) &= \int_V \sigma_{ij}\delta\epsilon_{ij}\,\mathrm{d}V - \int_V \lambda\overline{B}_i\delta u_i\,\mathrm{d}V - \int_S \lambda\overline{F}_i\delta u_i\,\mathrm{d}S - \sum_{k=1}^{n^k}\lambda\overline{R}_i^k\delta u_i^k \\
&= \int_V \sigma_{ij}\delta\epsilon_{ij}\,\mathrm{d}V - \int_\Omega \lambda\overline{T}_i\delta u_i\,\mathrm{d}\Omega = 0 \quad (13)
\end{aligned}
$$

Here $\overline{B}_i$, $\overline{F}_i$, and $\overline{R}_i$ are the load distributions for body, surface, and discrete loads, respectively, and they are collected in $\overline{T}_i$, where Ω defines definite integration. Using the Budiansky-Hutchinson notation the variation of the total potential energy is given by

$$
\delta\Pi(\boldsymbol{u}) = \boldsymbol{\sigma}\cdot\delta\boldsymbol{\epsilon} - \lambda\overline{\boldsymbol{T}}\cdot\delta\boldsymbol{u} = 0 \quad (14)
$$

By comparing Equation (13) and Equation (14), the $\cdot$ operator is defined as multiplication and definite integration. Equation (14) is valid in both a pre- and post-buckling configuration. To

determine the Koiter a- and b-factors, equations (4), (5), and (11) are inserted into Equation (14), and the terms are collected in powers of ξ as

$$
\begin{aligned}
&\lambda_c{}^0\boldsymbol{\sigma} \cdot l_1\left(\delta\boldsymbol{u}\right) - \lambda_c\overline{\boldsymbol{T}} \cdot \delta\boldsymbol{u} + \left[\lambda_c{}^0\boldsymbol{\sigma} \cdot l_{11}\left({}^1\boldsymbol{u}, \delta\boldsymbol{u}\right) + {}^1\boldsymbol{\sigma} \cdot l_1\left(\delta\boldsymbol{u}\right) + a\lambda_c\left({}^0\boldsymbol{\sigma} \cdot l_1\left(\delta\boldsymbol{u}\right) - \overline{\boldsymbol{T}} \cdot \delta\boldsymbol{u}\right)\right]\xi \\
&+ \left[\lambda_c{}^0\boldsymbol{\sigma} \cdot l_{11}\left({}^2\boldsymbol{u}, \delta\boldsymbol{u}\right) + \left(a\lambda_c{}^0\boldsymbol{\sigma} + {}^1\boldsymbol{\sigma}\right) \cdot l_{11}\left({}^1\boldsymbol{u}, \delta\boldsymbol{u}\right) + {}^2\boldsymbol{\sigma} \cdot l_1\left(\delta\boldsymbol{u}\right) + b\lambda_c\left({}^0\boldsymbol{\sigma} \cdot l_1\left(\delta\boldsymbol{u}\right) - \overline{\boldsymbol{T}} \cdot \delta\boldsymbol{u}\right)\right]\xi^2 \\
&+ \left[\lambda_c{}^0\boldsymbol{\sigma} \cdot l_{11}\left({}^3\boldsymbol{u}, \delta\boldsymbol{u}\right) + {}^3\boldsymbol{\sigma} \cdot l_1\left(\delta\boldsymbol{u}\right) + \left(a\lambda_c{}^0\boldsymbol{\sigma} + {}^1\boldsymbol{\sigma}_1\right) \cdot l_{11}\left({}^2\boldsymbol{u}, \delta\boldsymbol{u}\right)\right]\xi^3 \\
&+ \left[\left(b\lambda_c{}^0\boldsymbol{\sigma} + {}^2\boldsymbol{\sigma}\right) \cdot l_{11}\left({}^1\boldsymbol{u}, \delta\boldsymbol{u}\right) + c\lambda_c\left({}^0\boldsymbol{\sigma} \cdot l_1\left(\delta\boldsymbol{u}\right) - \overline{\boldsymbol{T}} \cdot \delta\boldsymbol{u}\right)\right]\xi^3 + \cdots = 0
\end{aligned}
\tag{15}
$$

This equation is valid for any value of ξ, hence each coefficient must be zero. This defines four problems providing all the data needed to perform the post-buckling analysis.

The zeroth order problem is the pre-buckling equilibrium equations, and is

$$
{}^0\boldsymbol{\sigma} \cdot l_1\left(\delta\boldsymbol{u}\right) - \overline{\boldsymbol{T}} \cdot \delta\boldsymbol{u} = 0
\tag{16}
$$

This term is present in all the higher order equations, see Equation (15), and can be removed from the system of equations. Reducing the first order problem by the zeroth order problem, the first post-buckling problem becomes

$$
{}^1\boldsymbol{\sigma} \cdot l_1\left(\delta\boldsymbol{u}\right) + \lambda_c{}^0\boldsymbol{\sigma} \cdot l_{11}\left({}^1\boldsymbol{u}, \delta\boldsymbol{u}\right) = 0
\tag{17}
$$

This is a linear eigenvalue buckling problem, and ${}^1\boldsymbol{u}$ is the corresponding buckling mode shape. The second order problem is used to obtain both the second post-buckling displacement field, ${}^2\boldsymbol{u}$, and the Koiter a-factor. The derivation of the ${}^2\boldsymbol{u}$ displacement field and the Koiter a-factor is reported several places in literature, e.g., [13, 14, 16, 20, 31], hence only the end results are restated here as

$$
{}^2\boldsymbol{\sigma} \cdot l_1\left(\delta\boldsymbol{u}\right) + \lambda_c{}^0\boldsymbol{\sigma} \cdot l_{11}\left({}^2\boldsymbol{u}, \delta\boldsymbol{u}\right) = -{}^1\boldsymbol{\sigma} \cdot l_{11}\left({}^1\boldsymbol{u}, \delta\boldsymbol{u}\right)
\tag{18}
$$

This problem is equivalent to Equation (17) with a pseudo load vector, however it is singular. The a-factor can be determined by

$$
a\lambda_c = -\frac{3}{2}\frac{{}^1\boldsymbol{\sigma} \cdot l_2\left({}^1\boldsymbol{u}\right)}{{}^0\boldsymbol{\sigma} \cdot l_2\left({}^1\boldsymbol{u}\right)}
\tag{19}
$$

As previously mentioned a is zero for symmetric buckling, and if it is non-zero the buckling is asymmetric. The last step is to determine the b-factor. The b factor can be determined from the third order problem.

$$
b\lambda_c = -\frac{{}^2\boldsymbol{\sigma} \cdot l_2\left({}^1\boldsymbol{u}\right) + 2{}^1\boldsymbol{\sigma}_1 \cdot l_{11}\left({}^1\boldsymbol{u}, {}^2\boldsymbol{u}\right)}{{}^0\boldsymbol{\sigma} \cdot l_2\left({}^1\boldsymbol{u}\right)}
\tag{20}
$$

Based on this the equations for conducting asymptotic post-buckling analysis assuming linear pre-buckling displacements have been derived.

3.2. Asymptotic post-buckling analysis in Finite Element form

To determine the governing equations needed in Finite Element Analysis, the Budiansky-Hutchinson operators are translated. Only Equations (16)-(20) are needed to perform the analysis. In the remainder of the paper ${}^k\mathbf{U}$ refer to the global nodal displacement vectors for displacement field k. Equation (16) is the linear static problem, and in Finite Element form is

$$
\mathbf{K}_0{}^0\mathbf{U} = \mathbf{R}
\tag{21}
$$

Here $\mathbf{K}_0$ is the linear stiffness matrix, ${}^0\mathbf{U}$ is the pre-buckling displacement vector, and $\mathbf{R}$ is the reference load vector. Equation (22) is the linear buckling problem given in Finite Element form as

$$
\left(\mathbf{K}_0 + \lambda_j\mathbf{K}_\sigma^0\right)\boldsymbol{\Phi}_j = \mathbf{0}, \quad j = 1, 2, \dots
\tag{22}
$$

Here $\mathbf{K}_\sigma^0$ is the global stress stiffness matrix where the superscript refer to the stress field used to calculate the stress stiffness matrix, $\boldsymbol{\Phi}_j$ is the eigenvector corresponding to buckling load factor

λ_j. The eigenvalues are assumed to be ordered with $\lambda_1 = \lambda_c < \lambda_2 \leq \lambda_3 \ldots \leq \lambda_n$ and we define $^1\mathbf{U} \equiv \boldsymbol{\Phi}_1$. The first post-buckling problem Equation (18) is in Finite Element form given as

$$\left(\mathbf{K}_0 + \lambda_c \mathbf{K}_\sigma^0\right) {}^2\mathbf{U} = \mathbf{Q} \tag{23}$$

The left hand side of Equation (23) is similar to Equation (22), hence is singular. The right hand side vector $\mathbf{Q}$ is the pseudo load vector given by Equation (24), and it is used to determine the post-buckling displacements $^2\mathbf{U}$,

$$\mathbf{Q} = -\left(\mathbf{K}_\sigma^1 + \frac{1}{2}\mathbf{K}_{0L}\right) {}^1\mathbf{U} \tag{24}$$

Here $\mathbf{K}_\sigma^1$ is calculated in the same manner as $\mathbf{K}_\sigma^0$ with the difference being that the $^1\boldsymbol{\sigma}$-stress field is used instead of the $^0\boldsymbol{\sigma}$-stress field. $\mathbf{K}_{0L}$ is an unsymmetric stiffness matrix which couples the non-linear l_2 operator to the linear l_1 operator, and is

$$\mathbf{K}_{0L} = \mathbf{K}_{0L}\left({}^1\mathbf{U}\right) = \sum_{e=1}^{n^e} \int_{V_e} \mathbf{B}_0^T \mathbf{E} \mathbf{B}_L\left({}^1\mathbf{U}^e\right) \mathrm{d}V \tag{25}$$

Here superscript ^{e} refers to an element quantity and the summation over all elements involves assembly to global level, $\mathbf{B}_0$ is the linear strain displacement matrix, $\mathbf{E}$ is the constitutive matrix, $\mathbf{B}_L\left({}^1\mathbf{U}^e\right)$ is the nonlinear strain-displacement matrix constructed using the buckling mode shape, V_e is the volume of the element, and n^e is the number of finite elements. The singularity from Equation (23) is removed by imposing the orthogonality condition: $\mathbf{L} = \mathbf{K}_0 {}^1\mathbf{U}$ using a perturbed Lagrangian method.

$$\begin{bmatrix} \mathbf{K}_0 + \lambda_c \mathbf{K}_\sigma^0 & \mathbf{L} \\ \mathbf{L}^T & -\varepsilon \end{bmatrix} \left\{ \begin{array}{c} {}^2\mathbf{U} \\ \mu \end{array} \right\} = \left\{ \begin{array}{c} \mathbf{Q} \\ 0 \end{array} \right\} \tag{26}$$

Here ε is the penalty factor. Through numerical studies, different choices of penalty factor did not show any effect on the analysis results, thus $\varepsilon = 1$ in this work. μ is the Lagrange multiplier. The orthogonality condition does not alter the skyline of the original matrix, hence the sparseness of the system matrix is unaltered. The displacement field is needed to calculate the Koiter a- and b-factors. The a-factor is given by

$$a\lambda_c = -\frac{3}{2} \sum_{e=1}^{n^e} \frac{\int_{V_e} \boldsymbol{\sigma}_1^T \mathbf{B}_L\left({}^1\mathbf{U}^e\right) \mathrm{d}V\, {}^1\mathbf{U}^e}{\int_{V_e} \boldsymbol{\sigma}_0^T \mathbf{B}_L\left({}^1\mathbf{U}^e\right) \mathrm{d}V\, {}^1\mathbf{U}^e} = -\frac{3}{2} \frac{{}^1\mathbf{U}^T \mathbf{K}_{0L} {}^1\mathbf{U}}{{}^0\mathbf{U}^T \mathbf{K}_{0L} {}^1\mathbf{U}} = -\frac{3 N^A\left({}^1\mathbf{U}\right)}{2 D\left({}^0\mathbf{U}, {}^1\mathbf{U}\right)} \tag{27}$$

N^A is the numerator for the $a\lambda_c$-factor, and D is the denominator for all Koiter factors. Finally, the b-factor is given by

$$b\lambda_c = -\sum_{e=1}^{n^e} \frac{\int_{V_e} \boldsymbol{\sigma}_2^T \mathbf{B}_L\left({}^1\mathbf{U}^e\right) \mathrm{d}V\, {}^1\mathbf{U}^e + 2 \int_{V_e} \boldsymbol{\sigma}_1^T \mathbf{B}_L\left({}^1\mathbf{U}^e\right) \mathrm{d}V\, {}^2\mathbf{U}^e}{\int_{V_e} \boldsymbol{\sigma}_0^T \mathbf{B}_L\left({}^1\mathbf{U}^e\right) \mathrm{d}V\, {}^1\mathbf{U}^e}$$

$$= -\frac{{}^2\mathbf{U}^T \mathbf{K}_{0L} {}^1\mathbf{U} + \frac{1}{2} {}^1\mathbf{U}^T \mathbf{K}_{LL} {}^1\mathbf{U} + 2 {}^1\mathbf{U}^T \mathbf{K}_{0L} {}^2\mathbf{U}}{D} = -\frac{N^B\left({}^1\mathbf{U}, {}^2\mathbf{U}\right)}{D\left({}^0\mathbf{U}, {}^1\mathbf{U}\right)} \tag{28}$$

Here N^B is the numerator for the $b\lambda_c$-factor and $\mathbf{K}_{LL}$ is a symmetric stiffness matrix relating the l_2-operator to the l_2-operator, and it is given by

$$\mathbf{K}_{LL} = \mathbf{K}_{LL}\left({}^1\mathbf{U}\right) = \sum_{e=1}^{n^e} \int_{V_e} \left(\mathbf{B}_L\left({}^1\mathbf{U}^e\right)\right)^T \mathbf{E} \mathbf{B}_L\left({}^1\mathbf{U}^e\right) \mathrm{d}V \tag{29}$$

The Koiter factors and sensitivities hereof are efficiently calculated by a summation of element contributions, hence the global $\mathbf{K}_{0L}$ and $\mathbf{K}_{LL}$ matrices should not be used, and they are only shown here for completeness.

4. DESIGN SENSITIVITY ANALYSIS FOR ASYMPTOTIC POST-BUCKLING

The objective of this work is to maximize the post-buckling stability of laminated composite structures by gradient-based optimization techniques. To perform design optimization of the post-buckling response, the design sensitivities of the Koiter factors, a and b, and the critical buckling load factor λ_c are needed. The direct differentiation method is used to derive the design sensitivities.

4.1. Sensitivity analysis of the pre-buckling displacement field

The linear pre-buckling displacements are used to calculate both Koiter factors and the critical buckling load factor, hence the sensitivities of the pre-buckling displacement field, $^0\mathbf{U}$, with respect to a set of generalized design variables x_i are needed. The sensitivities are determined by differentiation of Equation (21). Assuming design independent loads the sensitivities of the load vector are zero.

$$\mathbf{K}_0 \frac{\mathrm{d}^0\mathbf{U}}{\mathrm{d}x_i} = -\frac{\mathrm{d}\mathbf{K}_0}{\mathrm{d}x_i}{}^0\mathbf{U} + \underbrace{\frac{\mathrm{d}\mathbf{R}}{\mathrm{d}x_i}}_{\equiv 0} \tag{30}$$

The already factored stiffness matrix $\mathbf{K}_0$ can be reused for the calculation of the pre-buckling displacement sensitivities, thereby enhancing computational efficiency.

4.2. Sensitivity analysis of (simple) buckling load factors

The sensitivities of the pre-buckling displacement field are employed in the calculation of the design sensitivities of the buckling load factors. In this work only simple i.e., distinct buckling load factors are considered. The buckling load factor sensitivities are calculated by differentiating Equation (22), pre-multiplying by $\mathbf{\Phi}_j$, rearranging the equations, and assuming that the eigenvectors are $\mathbf{K}_\sigma^0$-orthonormalized.

$$\frac{\mathrm{d}\lambda_j}{\mathrm{d}x_i} = \mathbf{\Phi}_j^T \left(\frac{\mathrm{d}\mathbf{K}_0}{\mathrm{d}x_i} + \lambda_j \frac{\mathrm{d}\mathbf{K}_\sigma^0}{\mathrm{d}x_i} \right) \mathbf{\Phi}_j \tag{31}$$

Please note that $\dfrac{\mathrm{d}\mathbf{K}_\sigma^0}{\mathrm{d}x_i}$ is a function of the displacements, hence is dependent on all elements. Equation (31) is solved using semi-analytic design sensitivity analysis, this approach also facilitates easy implementation of different design variables [32]. It is important to note that the stress stiffness matrix is a function of both the design variables and the pre-buckling displacement field, hence $\mathbf{K}_\sigma^0 = \mathbf{K}_\sigma^0 \left(x_i, {}^0\mathbf{U}(x_i) \right)$. The sensitivities of $\mathbf{K}_0$ and $\mathbf{K}_\sigma^0$ are calculated using central differences at the element level [32, 33].

$$\frac{\mathrm{d}\mathbf{K}_0^e}{\mathrm{d}x_i} = \frac{\mathbf{K}_0^e\left(x_i + \Delta x_i\right) - \mathbf{K}_0^e\left(x_i - \Delta x_i\right)}{2\Delta x_i} \tag{32}$$

$$\frac{\mathrm{d}\mathbf{K}_\sigma^{0,e}}{\mathrm{d}x_i} = \frac{\mathbf{K}_\sigma^{0,e}\left(x_i + \Delta x_i, {}^0\mathbf{U}^e + \Delta^0\mathbf{U}^e\right) - \mathbf{K}_\sigma^{0,e}\left(x_i - \Delta x_i, {}^0\mathbf{U}^e - \Delta^0\mathbf{U}^e\right)}{2\Delta x_i} \tag{33}$$

The change in element displacements $\Delta^0\mathbf{U}^e$ is approximated using a first order Taylor expansion

$$\Delta^0\mathbf{U}^e \approx \frac{\mathrm{d}^0\mathbf{U}^e}{\mathrm{d}x_i} \Delta x_i$$

The first order Taylor expansion is also used when the changes in the displacement fields $\Delta^1\mathbf{U}$ and $\Delta^2\mathbf{U}$ are calculated.

4.3. Sensitivity analysis of (simple) eigenvectors

The sensitivities of a simple eigenvector $\mathbf{\Phi}_j$ cannot be determined by differentiation of Equation (22) because the system matrix is singular with a rank deficiency of 1. Instead Nelson's method [34] is applied to calculate the sensitivities. The principle in Nelson's method is to rescale the eigenvector and remove the singularity. The sensitivities of the original eigenvector are determined based on the

sensitivity of the scaled eigenvector. The scaled eigenvector $\mathbf{W}_j$ is determined by

$$\mathbf{W}_j = \frac{1}{q}\boldsymbol{\Phi}_j \tag{34}$$

Here q is chosen such that

$$\max_l \left| W_j^l \right| = W_j^m = 1, \quad l = 1, \dots, n^{DoF}$$

The entry with the maximum absolute value for eigenvector j is referred to as m and the component W_j^m. n^{DoF} is the number of degrees of freedom in the model. Recall from Section 4.2 that $\boldsymbol{\Phi}_j$ is $\mathbf{K}_\sigma^0$-orthonormalized, and by differentiation

$$\boldsymbol{\Phi}_j^T \left(-\mathbf{K}_\sigma^0\right) \frac{\mathrm{d}\boldsymbol{\Phi}_j}{\mathrm{d}x_i} = -\frac{1}{2}\boldsymbol{\Phi}_j^T \frac{\mathrm{d}\left(-\mathbf{K}_\sigma^0\right)}{\mathrm{d}x_i}\boldsymbol{\Phi}_j \tag{35}$$

To eliminate $\dfrac{\mathrm{d}\boldsymbol{\Phi}_j}{\mathrm{d}x_i}$ from Equation (35) Equation (34) is differentiated.

$$\frac{\mathrm{d}\boldsymbol{\Phi}_j}{\mathrm{d}x_i} = \frac{\mathrm{d}q}{\mathrm{d}x_i}\mathbf{W}_j + q\frac{\mathrm{d}\mathbf{W}_j}{\mathrm{d}x_i} \tag{36}$$

It is important to note that $\dfrac{\mathrm{d}q}{\mathrm{d}x_i} \neq 0$ in the general case since a change in $\mathbf{K}_\sigma^0$ affects the $\mathbf{K}_\sigma^0$-orthonormalization, hence the scaling required between $\boldsymbol{\Phi}_j$ and $\mathbf{W}_j$. To calculate $\dfrac{\mathrm{d}q}{\mathrm{d}x_i}$ Equation (36) is substituted into Equation (35), and $\dfrac{\mathrm{d}\boldsymbol{\Phi}_j}{\mathrm{d}x_i}$ is eliminated.

$$\frac{\mathrm{d}q}{\mathrm{d}x_i} = -q^2\boldsymbol{\Phi}_j^T\left(-\mathbf{K}_\sigma^0\right)\frac{\mathrm{d}\mathbf{W}_j}{\mathrm{d}x_i} - \frac{q}{2}\boldsymbol{\Phi}_j^T\frac{\mathrm{d}\left(-\mathbf{K}_\sigma^0\right)}{\mathrm{d}x_i}\boldsymbol{\Phi}_j \tag{37}$$

The unknown quantities are the rescaled eigenvector sensitivities $\dfrac{\mathrm{d}\mathbf{W}_j}{\mathrm{d}x_i}$. To obtain these, $\mathbf{W}_j$ is substituted into Equation (22), and the resulting expression is differentiated to become

$$\left(\mathbf{K}_0 + \lambda_c\mathbf{K}_\sigma^0\right)\frac{\mathrm{d}\mathbf{W}_j}{\mathrm{d}x_i} = -\mathbf{R}_{u1} \tag{38}$$

where the right hand side vector $\mathbf{R}_{u1}$ is given as

$$\mathbf{R}_{u1} = \left(\frac{\mathrm{d}\mathbf{K_0}}{\mathrm{d}x_i} + \lambda_c\frac{\mathrm{d}\mathbf{K}_\sigma}{\mathrm{d}x_i} + \frac{\mathrm{d}\lambda_c}{\mathrm{d}x_i}\mathbf{K}_\sigma\right)\mathbf{W}_j$$

This system is still singular. In order to remove the singularity the normalization condition of $\mathbf{W}_j$ is differentiated

$$\frac{\mathrm{d}W_j^m}{\mathrm{d}x_i} = 0 \tag{39}$$

This result is substituted into Equation (38) by changing the appropriate entries in $\mathbf{K}_0$, $\mathbf{K}_\sigma^0$, and $\mathbf{R}_{u1}$, i.e.,

$$\begin{aligned} &\mathbf{K}_0(m,k) = \mathbf{K}_\sigma^0(m,k) = \mathbf{K}_0(k,m) = \mathbf{K}_\sigma^0(k,m) = 0, \\ &\mathbf{K}_0(m,m) = 1, \qquad\qquad \mathbf{R}_{u1}(m) = 0, \end{aligned} \qquad k = 1, \dots, n^{DoF}, \qquad k \neq m$$

The new system matrix and pseudo load-vector are called $\mathbf{K}^{0,r}$ and $\mathbf{R}_{u1}^r$, respectively. This system of equations is not singular, and can be solved directly

$$\mathbf{K}^{0,r}\frac{\mathrm{d}\mathbf{W}_j}{\mathrm{d}x_i} = -\mathbf{R}_{u1}^r \tag{40}$$

When the sensitivities of $\mathbf{W}_j$ are obtained using Equation (40) these are substituted into Equation (37) and Equation (36). From this the eigenvector sensitivities $\dfrac{\mathrm{d}\boldsymbol{\Phi}_j}{\mathrm{d}x_i}$ are obtained. For $j = 1$ the sensitivities of the $^1\mathbf{U}$ displacement field are obtained.

4.4. Sensitivity analysis of the post-buckling displacement field

The sensitivities of the post-buckling displacement field $\dfrac{\mathrm{d}^2\mathbf{U}}{\mathrm{d}x_i}$ are used when determining the sensitivities of the Koiter b-factor. The post-buckling displacement field sensitivities are obtained in a similar manner as the pre-buckling displacement field sensitivities. Assuming that the buckling load and buckling mode shape sensitivities are known, the sensitivities of the $^2\mathbf{U}$ displacement field are obtained by differentiation of the extended system of equations, Equation (26)

$$
\begin{bmatrix}
\mathbf{K}_0 + \lambda_c \mathbf{K}_\sigma^0 & \mathbf{L} \\
\mathbf{L}^T & -\varepsilon
\end{bmatrix}
\left\{
\begin{array}{c}
\dfrac{\mathrm{d}^2\mathbf{U}}{\mathrm{d}x_i} \\
\dfrac{\mathrm{d}\mu}{\mathrm{d}x_i}
\end{array}
\right\}
= -
\left\{
\begin{array}{c}
\left(\dfrac{\mathrm{d}\mathbf{K}_0}{\mathrm{d}x_i} + \dfrac{\mathrm{d}\lambda_c}{\mathrm{d}x_i}\mathbf{K}_\sigma^0 + \lambda_c \dfrac{\mathrm{d}\mathbf{K}_\sigma^0}{\mathrm{d}x_i} \right)\,^2\mathbf{U} - \dfrac{\mathrm{d}\mathbf{Q}}{\mathrm{d}x_i} \\
\dfrac{\mathrm{d}\mathbf{L}^T}{\mathrm{d}x_i}\,^2\mathbf{U}
\end{array}
\right\}
\tag{41}
$$

The derivative $\dfrac{\mathrm{d}\mathbf{Q}}{\mathrm{d}x_i}$ is non-zero, and it is given as

$$
\frac{\mathrm{d}\mathbf{Q}}{\mathrm{d}x_i} = -\left(\frac{\mathrm{d}\mathbf{K}_\sigma^1}{\mathrm{d}x_i} + \frac{1}{2}\frac{\mathrm{d}\mathbf{K}_{0L}}{\mathrm{d}x_i} \right)\,^1\mathbf{U} - \left(\mathbf{K}_\sigma^1 + \frac{1}{2}\mathbf{K}_{0L} \right) \frac{\mathrm{d}\,^1\mathbf{U}}{\mathrm{d}x_i}
$$

Furthermore the sensitivities of the $\mathbf{L}$ vector are given as

$$
\frac{\mathrm{d}\mathbf{L}}{\mathrm{d}x_i} = \frac{\mathrm{d}\mathbf{K}_0}{\mathrm{d}x_i}\,^1\mathbf{U} + \mathbf{K}_0 \frac{\mathrm{d}\,^1\mathbf{U}}{\mathrm{d}x_i}
$$

The extended system of equations in Equation (41) is not singular, and the post-buckling sensitivities are obtained by back-substitution.

4.5. Sensitivity analysis of Koiter a-factor

The sensitivity of Equation (27) yields the change in asymmetry of the post-buckling response, and are determined by

$$
\frac{\mathrm{d}(a\lambda_c)}{\mathrm{d}x_i} = -\frac{3}{2}\frac{\dfrac{\mathrm{d}N^A}{\mathrm{d}x_i}D - N^A\dfrac{\mathrm{d}D}{\mathrm{d}x_i}}{D^2}
\tag{42}
$$

The sensitivities of N^A and D are given in Equation (43) and (44), respectively, as

$$
\frac{\mathrm{d}N^A}{\mathrm{d}x_i} = \left(^1\mathbf{U}^T \frac{\mathrm{d}\mathbf{K}_{0L}}{\mathrm{d}x_i} + \frac{\mathrm{d}\,^1\mathbf{U}^T}{\mathrm{d}x_i}\left(\mathbf{K}_{0L} + \mathbf{K}_{0L}^T \right) \right)\,^1\mathbf{U}
\tag{43}
$$

The sensitivities of $\mathbf{K}_{0L}$ are obtained by central differences in the same manner as Equation (33). The sensitivities of D are determined in the same manner as N^A

$$
\frac{\mathrm{d}D}{\mathrm{d}x_i} = ^0\mathbf{U}^T \frac{\mathrm{d}\mathbf{K}_{0L}}{\mathrm{d}x_i}\,^1\mathbf{U} + \frac{\mathrm{d}\,^0\mathbf{U}^T}{\mathrm{d}x_i}\mathbf{K}_{0L}\,^1\mathbf{U} + ^0\mathbf{U}^T\mathbf{K}_{0L}\frac{\mathrm{d}\,^1\mathbf{U}}{\mathrm{d}x_i}
\tag{44}
$$

The sensitivities of the a-factor are obtained by expanding the left hand side of Equation (42) and isolating $\dfrac{\mathrm{d}a}{\mathrm{d}x_i}$

$$
\frac{\mathrm{d}a}{\mathrm{d}x_i} = \frac{\dfrac{\mathrm{d}(a\lambda_c)}{\mathrm{d}x_i} - a\dfrac{\mathrm{d}\lambda_c}{\mathrm{d}x_i}}{\lambda_c}
\tag{45}
$$

The sensitivities are efficiently calculated by a summation on the element level.

4.6. Sensitivity analysis of Koiter b-factor

The sensitivities of the Koiter b-factor are calculated in the same manner as the a-factor, see Equation (42) and (45), and they are

$$\frac{\mathrm{d}(b\lambda_c)}{\mathrm{d}x_i} = -\frac{\dfrac{\mathrm{d}N^B}{\mathrm{d}x_i}D - N^B\dfrac{\mathrm{d}D}{\mathrm{d}x_i}}{D^2} \tag{46}$$

$$\frac{\mathrm{d}b}{\mathrm{d}x_i} = \frac{\dfrac{\mathrm{d}(b\lambda_c)}{\mathrm{d}x_i} - b\dfrac{\mathrm{d}\lambda_c}{\mathrm{d}x_i}}{\lambda_c} \tag{47}$$

The sensitivities of N^B are the only unknown quantities, and are

$$\frac{\mathrm{d}N^B}{\mathrm{d}x_i} = \left(^2\mathbf{U}^T\left(\frac{\mathrm{d}\mathbf{K}_{0L}}{\mathrm{d}x_i} + 2\frac{\mathrm{d}\mathbf{K}_{0L}^T}{\mathrm{d}x_i}\right) + \frac{1}{2}\,^1\mathbf{U}^T\frac{\mathrm{d}\mathbf{K}_{LL}}{\mathrm{d}x_i}\right)\,^1\mathbf{U} + \frac{\mathrm{d}^2\mathbf{U}^T}{\mathrm{d}x_i}\left(\mathbf{K}_{0L} + 2\mathbf{K}_{0L}^T\right)\,^1\mathbf{U}$$
$$+ \left(^2\mathbf{U}^T\left(\mathbf{K}_{0L} + 2\mathbf{K}_{0L}^T\right) + \,^1\mathbf{U}^T\mathbf{K}_{LL}\right)\frac{\mathrm{d}^1\mathbf{U}}{\mathrm{d}x_i} \tag{48}$$

$\dfrac{\mathrm{d}\mathbf{K}_{LL}}{\mathrm{d}x_i}$ is calculated in the same manner as $\dfrac{\mathrm{d}\mathbf{K}_{0L}}{\mathrm{d}x_i}$. All the derived expressions have been validated using finite difference approximations.

5. ASYMPTOTIC POST-BUCKLING OBJECTIVE FUNCTIONS

The Koiter factors are used to optimize the initial post-buckling response of all structures considered.

When the bifurcation is symmetric $a = 0$ and the initial post-buckling response is governed by the Koiter b-factor. To maximize the post-buckling stability we consider maximization of the Koiter b-factor. This formulation is

$$\text{Objective:} \quad \max_{x_i}\ b \tag{49}$$

$$\text{Subject to:} \quad \underline{x} \leq x_i \leq \overline{x} \quad \forall i \tag{50}$$

$$|a| \leq \overline{a} \tag{51}$$

$$\lambda_c \geq \underline{\lambda_1} \tag{52}$$

$$\lambda_j \geq \underline{\lambda_2} \quad j = 2, 3, \ldots \tag{53}$$

$$\left(\mathbf{K}_0 + \lambda_j\mathbf{K}_\sigma^0\right)\mathbf{\Phi}_j = \mathbf{0} \tag{54}$$

This formulation only considers the post-buckling curvature factor i.e., the Koiter b-factor, in the objective as this factor defines the post-buckling stability. Equation (50) prescribes the bounds on the design variables, which in the case of CFAO should be selected such that these are not reached in the optimization process. We have chosen the bounds to be the initial angle $\pm 180.9°$. These bounds are only used when calculating the move limits in the optimization. If asymmetric buckling is encountered a constraint on the maximum a-factor can be applied, see Equation (51). In Equation (52) a constraint on the critical buckling load factor can be applied to ensure that the structure does not buckle at a low load, the lowest acceptable buckling load factor $\underline{\lambda_1}$ can be determined as a fraction of the optimum buckling load factor from a buckling load maximization procedure. To avoid that the critical buckling load factor is multiple, Equation (53) is used. In the equation, $\underline{\lambda_2}$ is the minimum acceptable value of the buckling load factors larger than the critical one. The buckling problem in Equation (54) is not included directly into the optimization, but is solved explicitly prior to the solution of the optimization problem, hence a nested approach is used in this work.

An alternative approach is to maximize the $b\lambda_c$ product, as the product is present in the expansion of the load factor. This formulation is

$$\text{Objective:} \quad \max_{x_i} \ b\lambda_c \tag{55}$$

$$\text{Subject to:} \quad \underline{x} \leq x_i \leq \overline{x} \quad \forall i \tag{56}$$

$$|a| \leq \overline{a} \tag{57}$$

$$\lambda_j \geq \underline{\lambda_2} \quad j = 2, 3, \ldots \tag{58}$$

$$\left(\mathbf{K}_0 + \lambda_j \mathbf{K}_\sigma^0 \right) \mathbf{\Phi}_j = \mathbf{0} \tag{59}$$

In this formulation, the critical buckling load factor, λ_c, is implicitly maximized in the objective function, see Equation (55), hence a constraint on the critical buckling load factor is not applied. The remainder of the constraints are the same as the constraints in Equations (50)-(54). The difference between the two formulations is whether the critical buckling load factor is considered in the objective or not, and thus whether only the post-buckling curvature factor or a trade-off between the curvature factor and the critical buckling load factor should be considered.

When an asymmetric post-buckling response is present the Koiter a-factor is non-zero. Consequently the initial post-buckling response is unstable. In order to minimize the asymmetry the a-factor should be as close to zero as possible. Here, we minimize the absolute value of the a-factor given by Equations (60)-(64).

$$\text{Objective:} \quad \min_{x_i} \ |a| \tag{60}$$

$$\text{Subject to:} \quad \underline{x} \leq x_i \leq \overline{x} \quad \forall i \tag{61}$$

$$b \geq \underline{b} \tag{62}$$

$$\lambda_c \geq \underline{\lambda_1} \tag{63}$$

$$\left(\mathbf{K}_0 + \lambda_j \mathbf{K}_\sigma^0 \right) \mathbf{\Phi}_j = \mathbf{0} \tag{64}$$

The absolute value of the a-factor is considered in Equation (60). This is done because a negative a-factor still provides an asymmetric response, since the perturbation factor ξ in Equation (4) can be assigned with the opposite sign. This objective function is non-differentiable at $|a| = 0$, but the chance of reaching zero is negligibly small, and compared to using e.g., a^2 as objective, $|a|$ yields a better scaling of the optimization problem when $|a| < 1$, and thus should show better precision. Minimizing the absolute a-factor can affect the post-buckling curvature, and thus Equation (62) can be applied to constrain the Koiter b-factor, thereby securing a minimum post-buckling curvature.

Lastly, we also consider maximization of the critical buckling load factor. This optimization is used to gain a benchmark on the performance of the considered structures. The optimization problem is formulated using a bound formulation to ensure continuous derivatives [35, 36]

$$\text{Objective:} \quad \max_{x_i, \beta} \ \beta \tag{65}$$

$$\text{Subject to:} \quad \beta - \lambda_j \leq 0 \quad \forall j \tag{66}$$

$$\underline{x} \leq x_i \leq \overline{x} \quad \forall i \tag{67}$$

$$\left(\mathbf{K}_0 + \lambda_j \mathbf{K}_\sigma^0 \right) \mathbf{\Phi}_j = \mathbf{0} \tag{68}$$

In Equation (65) and (66) β is the bound variable. Applications of the optimization formulations are demonstrated in the following sections.

6. SIMPLY SUPPORTED SQUARE PLATE

The first example is the square plate shown in Figure 1 with dimensions and load given in Table I. The plate is simply supported along all four edges. The load is applied as a displacement along edge 1 to ensure that the edge remains straight under loading. The three remaining edges are forced
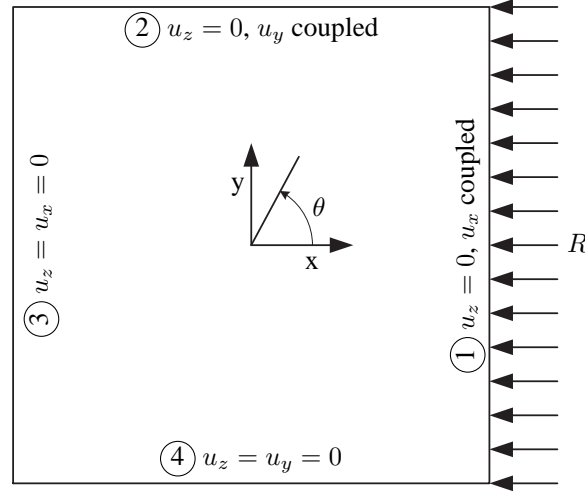
Figure 1. Load and supports for square plate. Coupled defines a side where the edge is forced straight but free to expand and contract. The load R is applied as a displacement along the edge. The encircled numbers refer to the edge number.

Table I. Dimensions and load for the square plate.

Parameter	Unit	
Side length, l	[m]	1.0
Thickness, t	[m]	0.002
Load, R	[kN]	1.0

Table II. Material properties for the glass fiber reinforced polymer used in the plate.

Parameter	Unit	
E_x	[GPa]	30.6
E_y	[GPa]	8.7
G_{xy}, G_{xz}	[GPa]	3.24
G_{yz}	[GPa]	2.9
ν_{xy}	[-]	0.29

straight by restraining the normal displacement on edges 3 and 4, and by coupling the normal displacement along edge 2, such that u_y is free to expand and contract, but the displacements remain the same, see Figure 1. As a consequence, the plate is free to expand and contract in the y-direction. The material used for the plate is a glass fiber reinforced polymer with material properties given in Table II. The plate is modeled using 400 9-noded shell elements based on a first order shear deformation theory. This mesh provides a converged solution with respect to displacements, stresses, and Koiter factors. The mesh is also sufficient to represent the more complicated stress fields from the optimized structures. No special measures were taken to avoid locking of the isoparametric shell finite elements used. This problem is circumvented by having a sufficiently fine mesh which has been verified by mesh refinement studies. The elements are grouped into 10×10 patches i.e., four elements per patch. Within a patch, the elements are forced to have the same fiber orientation. No restrictions on the fiber angles between the patches are enforced.

The fiber angles θ are used as design variables for the optimizations, and the convergence criterion is chosen to be $\sqrt{\dfrac{\sum_{i=1}^{n^e} \Delta\theta_i^2}{\sum_{i=1}^{n^e} \left(\overline{\theta}_i - \underline{\theta}_i\right)^2}} < 0.00001$ or the optimization is stopped after a maximum of 200 design iteration steps. The method of moving asymptotes (MMA) from [37] is chosen as optimizer. All numerical results are generated using the in-house finite element based analysis and design optimization code MUST (the MUltidisciplinary Synthesis Tool) [38].

6.1. Analysis of the plate

To validate the code, and obtain further insight into the problem, a series of analyses are carried out prior to conducting the post-buckling optimization.
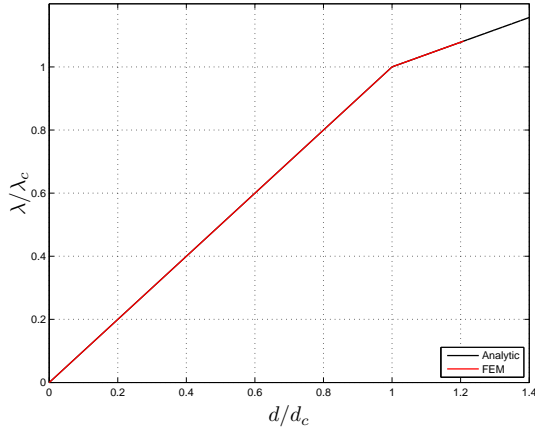
Figure 2. Normalized load-end shortening response for the analytical model given in Eqs. (69) and the implementation of Koiter's method using the Finite Element Method. All fiber angles are equal to $0°$ in the comparison.
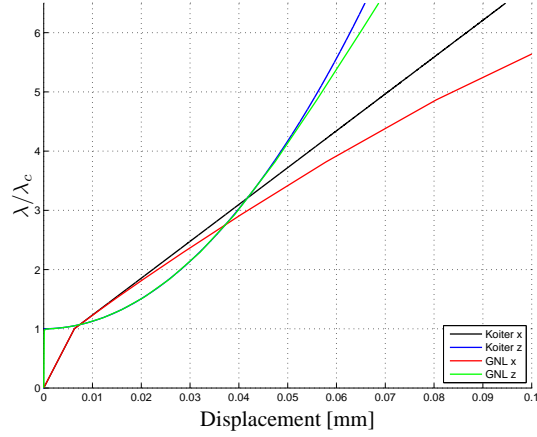
Figure 3. Comparison between Koiter analysis and geometrically non-linear analysis, GNL, for all fiber angles equal to $0°$. Displacement refers to either the end shortening, Koiter x and GNL x, or 1/100 of the normal deflection for the center node, Koiter z and GNL z. The load has been normalized with respect to the critical buckling load factor.

Analytical results exist for the load-end shortening of the square plate for orthotropic materials. Ref. [21] generalizes the results from [39] by removing the constraint on the post-buckling mode shape, and obtained Equation (69) for the load-end shortening response of the structure

$$R\lambda_c = \frac{\pi^2 t^3}{12 l_x^2 l_y^3 m^2 (\alpha \nu_{yx}^2)} \left(E_x \alpha^2 l_x^4 n^4 + E_x \alpha l_y^4 m^4 + \left\{ 2E_x \alpha \nu_{yx} + 4G_{xy} \left[\alpha - \nu_{yx}^2 \right] \right\} l_x^2 l_y^2 m^2 n^2 \right)$$

$$Rb\lambda_c = \frac{E_x \pi^2 t \left(\alpha l_x^4 n^4 + l_y^4 m^4 \right)}{16 l_x^2 l_y^3 m^2}, \quad \frac{u_0}{R} = -\frac{l_x}{t E_x l_y}, \quad u_2 = -\frac{l_x}{8} \left\{ \frac{m\pi}{l_x} \right\}^2$$

$$(69)$$

where l_x and l_y are the plate side lengths in the x and y directions, respectively. m and n are the number of half waves in the plate, α is the ratio between E_y and E_x, and ν_{yx} is the minor Poisson's ratio. In Figure 2 a comparison between the analytic results and the numerical method is shown. Good correlation between the models is observed.

Figure 3 compares the Koiter analysis to a geometrically non-linear (GNL) analysis. This study gives an estimate of the range of validity for the Koiter analysis. It is immediately observed that the out-of-plane displacement is better approximated than the end shortening. This result is as expected, because the in-plane displacements in the small deflection plate theory are given by the derivative of the out-of-plane displacements plus the in-plane displacements from the load. Because of that, the error in out-of-plane displacements in the Koiter analysis accumulates in the end shortening curve. Additionally, the Koiter analysis does not capture the softening behavior of the GNL analysis in the post-buckling region. This limitation is caused by the small number of terms included in the expansion, and the precision increases when additional terms are included, as demonstrated in e.g., [22]. Even though only the two first expansion parameters are included in the analysis, the error in displacements for the Koiter analysis is within 5% of the non-linear solution at a load factor of approximately $6.5\lambda_c$ and $2.2\lambda_c$ for the out-of-plane and end shortening displacements, respectively. The buckling mode shape is shown in Figure 4 and the x-component of the post-buckling mode shape in Figure 5. The post-buckling displacement field is a bi-axial contraction with the y-component identical to a rotation of $90°$ of the x-component.

To generate a qualitative overview of the response of the plate, surface plots of the critical buckling load factor λ_c and the Koiter b-factor are shown. These plots are generated using two patches, i.e., one for the elements with a negative y-coordinate, θ_1, and one design variable for the elements with a positive y-coordinate, θ_2. A Koiter analysis is conducted for all angles between $\pm 90°$ with an interval of $5°$. The surfaces are shown in Figures 6 and 7 for λ_c and b, respectively.

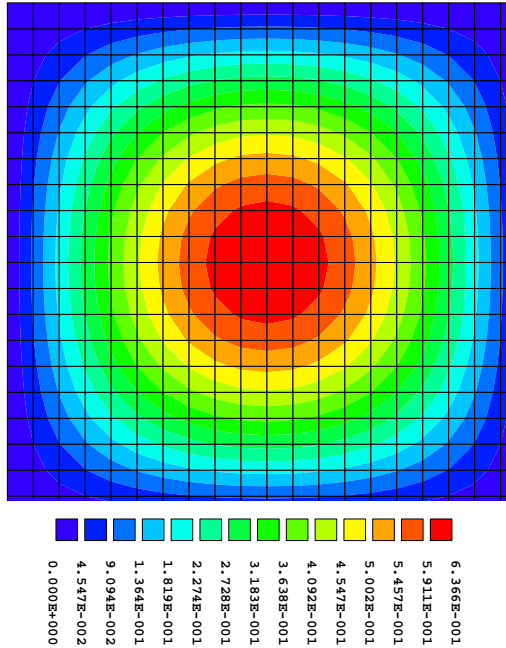Figure 4. Z-component of the buckling mode shape, $^1\mathbf{U}$, for the plate with all fiber angles aligned at $0°$.
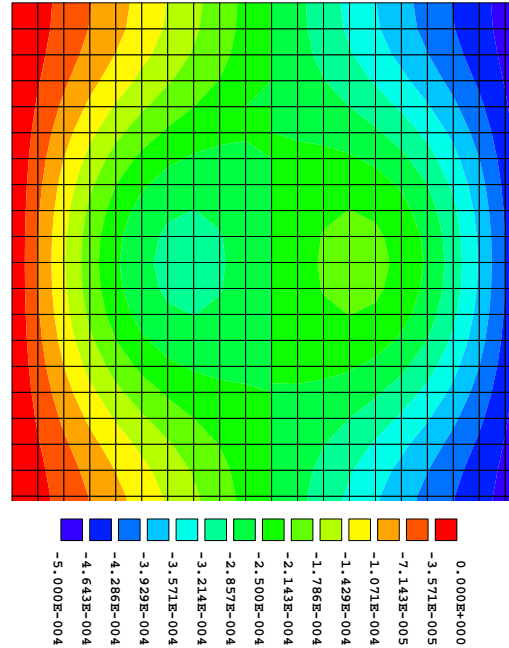

Figure 5. X-component of the post-buckling mode shape, $^2\mathbf{U}$, for the plate with all fibers aligned at $0°$. The y-component is identical when a $90°$ counterclockwise rotation is performed. The z-component is zero for all nodes.

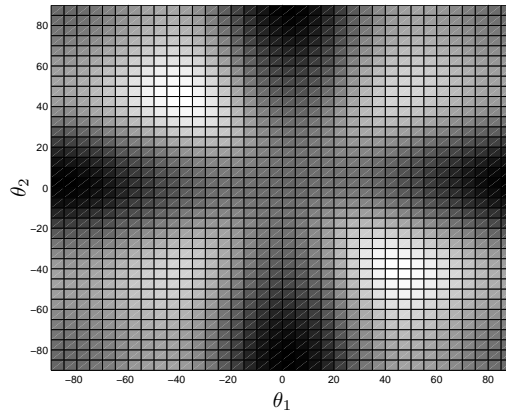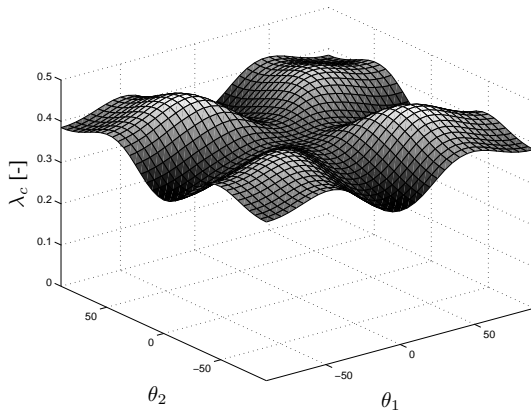Figure 6. Surface plot of the critical buckling load factor, λ_c, as a function of the fiber angles θ_1 and θ_2. Two weak global maxima are present i.e., $\theta_1 = -\theta_2 = \pm 45°$, furthermore two local maxima are located at $\theta_1 = \theta_2 = \pm 45°$. Nine minima are present with the global minima being any combination between $0°$ and $\pm 90°$. Local minima are present at $\theta_1 = \theta_2 = 0°$, $\theta_1 = \theta_2 = \pm 90°$, and $\theta_1 = -\theta_2 = \pm 90°$. Left isometric view, right top view.

It can be realized from the figures that the optimizations are non-convex with several local maxima, and that the global optimum is multiple in the case of two design variables. Furthermore, having two design variables then the maxima for one function corresponds to minima for the other function. Note that a global maximum in one function is not necessarily affine with a global minimum in the other function. A lower buckling load for the optimized structure is to be expected when optimizing the post-buckling stability compared to maximizing the buckling load.
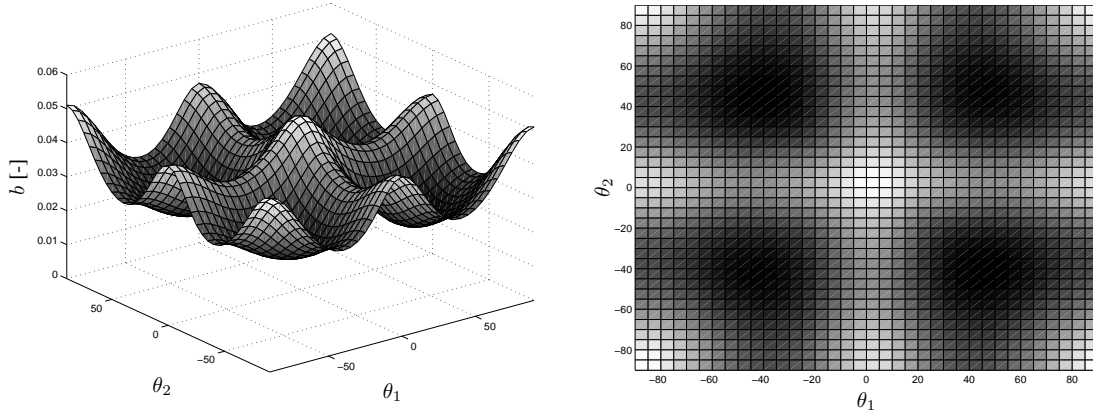
Figure 7. Surface plot of the Koiter b-factor as a function of the fiber angles θ_1 and θ_2. Five weak global maxima are present at $\theta_1 = \theta_2 = 0°$, $\theta_1 = \theta_2 = \pm 90°$, and $\theta_1 = -\theta_2 = \pm 90°$ and four local maxima are present at any combination between $0°$ and $\pm 90°$. The weak global minima are present at $\theta_1 = -\theta_2 = \pm 45°$ and the local minima at $\theta_1 = \theta_2 = \pm 45°$. Left isometric view, right top view.

6.2. *Buckling load optimization*

The single layered clamped square plate is chosen as the first example to demonstrate the capabilities of the proposed method. This example is simple, yet it demonstrates the differences between the different formulations.

Initially buckling load maximization is carried out. From this the upper bound on the buckling load is obtained, in order to have a baseline for comparing the results from the Koiter optimization. Furthermore, the maximum buckling load is used to formulate the constraints in Equations (52), (53), and (58). The optimum move-limit strategy and initial fiber angles for the buckling load maximization were determined by testing the 12 combinations of initial move limits (1%, 5%, and 10%) and initial fiber angles (0°, -45°, 45°, and 90°). The optimum combination of move-limit and initial angle was found to be 5% move-limits and an initial angle of 0° with an optimum buckling load factor $\lambda_c = 0.8241$ [-]. The optimum fiber angles are shown in Figure 8. The layup is symmetric around both the x- and y-axis even though no symmetry constraints have been applied in the optimization. The fiber angles are aligned close to either 0°, $\pm 45°$, or 90° with a $\pm 45°$ majority. The 0° patches are located along edge 2 and 4, and the 90° patches around the y-axis. The remainder of the structure consists of $\pm 45°$ patches which is in good agreement with the general theory for buckling of orthotropic plates stating that the optimum fiber angle for a single patch plate with the given boundary conditions is 45°. The two lowest buckling loads are located within 0.1%, and thus care must be taken to avoid multiple buckling loads during the post-buckling optimization.

6.3. *Post-buckling optimization*

Both post-buckling formulations with and without buckling load constraints are demonstrated for the plate. For both optimizations it is generally observed that using the optimum fiber angles from the buckling load maximization provides a good initial start guess for the post-buckling optimization compared to using initial fiber angles aligned at 0°, $\pm 45°$, or 90°. Initially the post-buckling stability is optimized without considering constraints on the buckling load factors.

Optimizing the post-buckling stability results in a decreased buckling load for most structures compared to the maximum attainable value as demonstrated in Figure 6 and 7. Furthermore, since the optimization problem is non-convex, different initial angles result in different optima. This is demonstrated in Table III where a maximization of the Koiter b-factor is conducted. Differences in both the critical buckling load factor and the b-factor are present. For this specific set of initial angles, a larger critical buckling load factor also result in an increased b-factor. This is not a general tendency, but rather a consequence of the choice of initial angle. In Figure 6 and Figure 7 it is
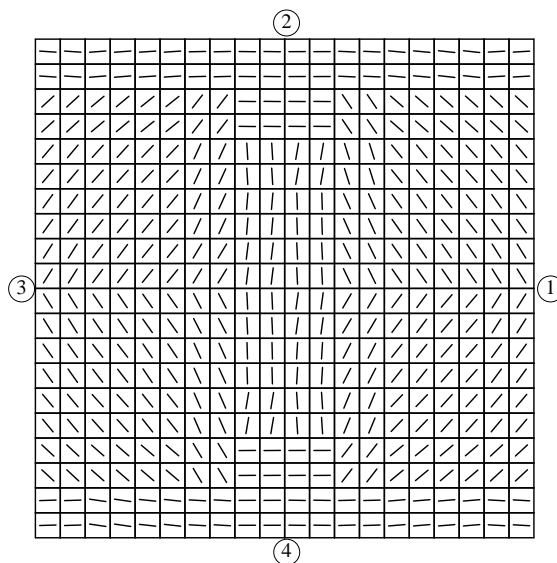
Figure 8. Optimum fiber angles for buckling load maximization of the single layer square plate. The settings used to obtain this result are 5% move-limits and an initial angle of $0°$.

Table III. Optimization results for maximizing the b-factor for the square plate with different initial angles and no buckling load constraint. The first column defines the initial angles, where λ_c corresponds to the initial angles given by the buckling load maximization, see Figure 8. The second and third columns are the first, λ_c, and second, λ_2, buckling loads, respectively. The fourth column is the Koiter b-factor, and the fifth column is the $b\lambda_c$-product. The second to fifth columns are the same throughout the plate example. All results are obtained using move-limits of 10%. Choosing move-limits of 1% and 5% yield results close to the ones presented in this table.

Initial angle	λ_c [-]	λ_2 [-]	b [-]	$b\lambda_c$ [-]
$0°$	0.3632	0.8666	0.06910	0.02510
$-45°$ / $45°$	0.4807	0.7299	0.07645	0.03675
$90°$	0.3154	0.4930	0.05913	0.01865
From max λ_c	0.5759	0.6277	0.07902	0.04551

observed that a global maxima in one of the functions can be affine with a local minima in the other which explains the obtained results. This example demonstrates the complicated response surface for the optimization.

The largest objective function values for the unconstrained optimizations were obtained with fiber angles from Figure 8 and move-limits of 10%. The results are given in Table IV. $0°$ is the optimum fiber angle with respect to post-buckling stiffness if a single fiber angle is selected, and together with the buckling load maximized design, Max λ_c, provide the baseline designs. Max b and Max $b\lambda_c$ are the unconstrained optimized designs for the optimization problems given by Equations (49)-(54) and Equations (55)-(59), respectively. The buckling loads are decreased by 30% and 15% for the two cases compared to the buckling optimized structure, respectively. Furthermore, the effect of the post-buckling optimization can be assessed by comparing the Koiter b-factor and the $b\lambda_c$-factor to the $0°$ case. The optimization results in an increase in the b-factor by 55% and 40% and the $b\lambda_c$-factor by 133% and 155% for the two optimizations, respectively. The difference between the two optimization formulations is also evident from this optimization. The Koiter b-factor is naturally larger for the first optimization formulation, whereas the $b\lambda_c$-factor is larger for the second optimization formulation. This is an important result as it shows that the two design spaces are not the same, and thus the choice of post-buckling optimization formulation affects the final result, even though the two formulations are closely related.

Figure 9 is used to explain the general tendencies observed in the post-buckling optimized designs. The bottom and top row of patches have an orientation close to $0°$. In the pre-buckling state

Table IV. Optimization results for the square plate without buckling load constraints and initial angles given by Figure 8. $0°$ represents the plate with all fiber angles aligned at $0°$. Max λ_c is the buckling load maximized plate, optimization problem given by Equations (65)-(68), Max b is the plate with maximized Koiter b-factor, optimization problem given by Equations (49)-(54), and lastly Max $b\lambda_c$ represents the plate with maximized Koiter $b\lambda_c$-factor, optimization problem given by Equations (55)-(59).

Case	λ_c [-]	λ_2 [-]	b [-]	$b\lambda_c$ [-]
$0°$	0.3846	0.9651	0.05109	0.01965
Max λ_c	0.8241	0.8249	0.03861	0.03182
Max b	0.5759	0.6277	0.07902	0.04551
Max $b\lambda_c$	0.7025	0.7032	0.07135	0.05012
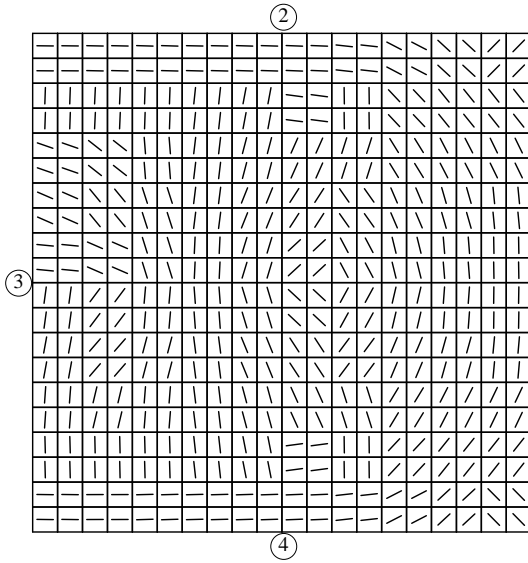
Figure 9. Optimum fiber angles for the Max b case for the square plate. The settings used to obtain this result are 10% move-limits and the initial angles from Figure 8.
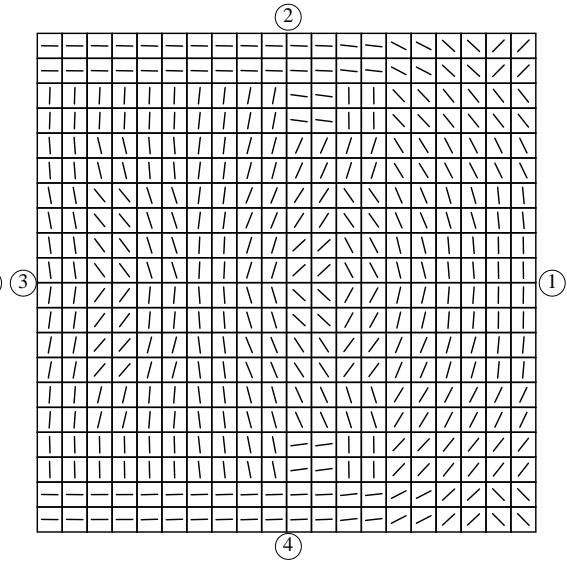
Figure 10. Modified fiber angles for the Max b case in Figure 9. These fiber angles gives a marginal increase in the b-factor of 0.3%.

these patches transfer the load to the supported edge and provide stiffness against the end-shortening of the plate. Furthermore, a $0°$ oriented element provides post-buckling stability, as it prevents the end shortening of the plate caused by the applied load and the post-buckling displacement field, $^2\mathbf{U}$. Close to, and at the loaded edge, the patches are oriented at $90°$ at y = 0 [mm] and $\mp45°$ at y = $\pm l/2$ with a smooth transition in between. This is used to redistribute the applied load towards the edges i.e., the $0°$ patches. The remaining $90°$ patches prevents the post-buckling contraction of the plate, and thus increase the post-buckling stability of the plate. The remaining patches are oriented at approximately $\pm45°$. These patches primarily provide resistance against buckling of the plate.

A symmetric layup about the x-axis is expected since the plate, boundary conditions, and discretization are symmetric. Yet the optimized fiber angles are not completely symmetric. The unsymmetry arises from the two columns of patches closest to edge 3. The $\sim0°$ patches located between y = 0 [mm] and y = 300 [mm] are assumed to be suboptimal, as these patches transfer the reaction force into the center of the plate. To demonstrate that it is the case, the corresponding patches with a negative y coordinate are mirrored to the suboptimal patches, see Figure 10. This results in a marginal increase in the b-factor of 0.3%, and an increase in the critical buckling load of 4%. Since the optimization only considers the b-factor the optimized design after 200 iterations is close to the results from a post-processed symmetric design. The marginal increase in the b-factor suggests that the design space is relatively flat, and that we can add additional constraints without a large reduction in the post-buckling performance.
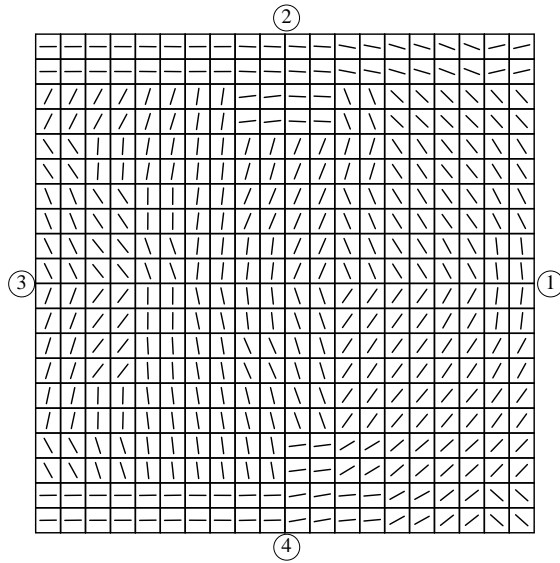
Figure 11. Optimum fiber angles for the Max $b\lambda_c$ case for the square plate. The settings used to obtain this result are 10% move-limits and the initial angles from Figure 8.
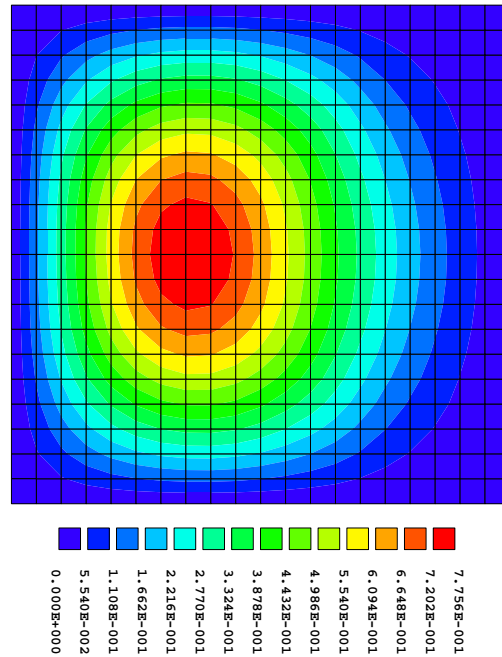

Figure 12. Z-component of a typical buckling mode shape for the post-buckling optimized plate. Compared to the buckling load optimized plate the buckle is shifted away from the loaded edge, furthermore, the buckle has a more oval shape caused by the boundary conditions. The buckling mode shape shown here is for the Max b case from Table IV. As the critical buckling load is increased towards the maximum attainable, the buckling mode shape approaches that of the buckling load maximized structure, i.e., a single round buckle in the center of the plate.

The optimized design for the Max $b\lambda_c$ case is given in Figure 11. The same general tendencies for the fiber angles are observed when comparing to the Max b case. The fiber angles resemble those from Figure 9 with more patches oriented at $\pm 45°$ in order to provide additional resistance against buckling.

The buckling mode shape for the Max b case is given in Figure 12. Compared to the initial structure i.e., all fiber aligned at $0°$, the buckling mode shape is shifted towards edge 3. The buckle is located in the area dominated by $90°$ patches. This is as expected since the $90°$ patches prevents the development of the buckle in the post-buckling regime. This result is obtained without any constraints on the fiber angles. If a symmetric response is required, constraints enforcing symmetry can be added.

6.4. Constraint on the critical buckling load factor

The critical buckling load factor is reduced when performing post-buckling optimization. To ensure a minimum buckling load factor minimum value constraints can be applied. The buckling load factor for the Max b case is 70% of the maximum attainable, and thus constraint values of 75%, 85%, and 90% of the maximum attainable critical buckling load factor are chosen to demonstrate the effect of constraining the critical buckling load factor when maximizing the b-factor. The constraint on the critical buckling load factor is only demonstrated with the optimization of the b-factor as the $b\lambda_c$-factor explicitly contains the critical buckling load factor in the objective function. The results for the optimizations are given in Table V. The consequences of the constraint on the critical buckling

Table V. Optimization results for the square plate with constraint on the critical buckling load. The constraints are formulated based on the maximum buckling load, and the subscript after b defines the percentage used in the constraint. The initial angles are given by Figure 8 and move-limits of 10%. The critical buckling load constraint for the 85% case is the value obtained when maximizing the $b\lambda_c$-factor, see Table IV. All results are maximization of the b-factor.

Case	λ_1 [-]	λ_c [-]	λ_2 [-]	b [-]	$b\lambda_c$ [-]
Max b_{75}	0.6180	0.6265	0.6291	0.07674	0.04808
Max b_{85}	0.7025	0.7025	0.7043	0.06991	0.04911
Max b_{90}	0.7417	0.7417	0.7424	0.06241	0.04629
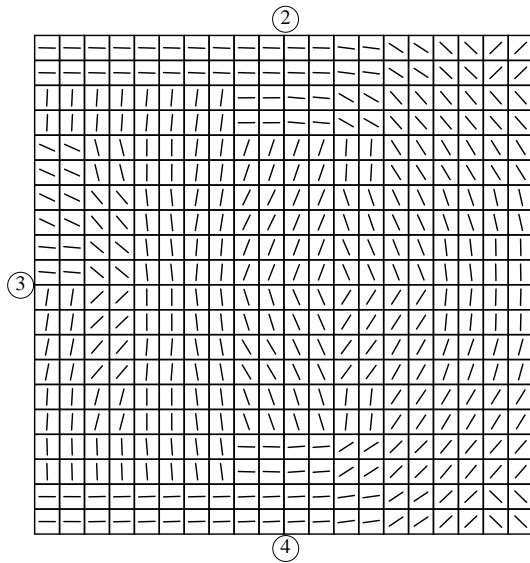
Figure 13. Optimum fiber angles for the Max b_{75} case i.e., with a constraint on the critical buckling load factor of 0.6180 for the plate. The settings used to obtain this result are 10% move-limits and the initial angles from Figure 8.
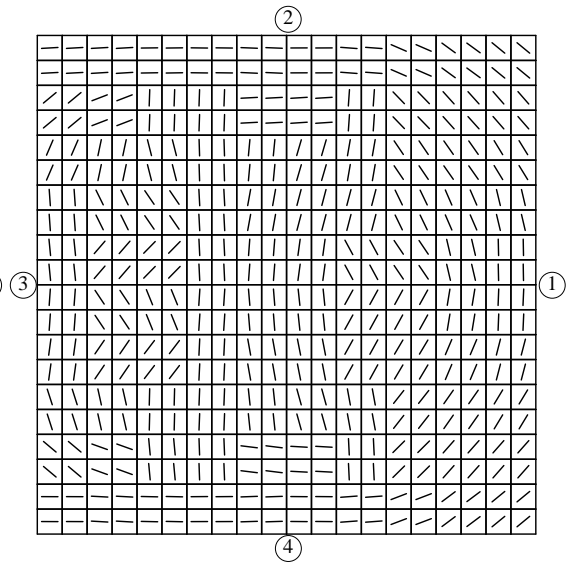
Figure 14. Optimum fiber angles for the Max b_{85} case where a constraint on the critical buckling load factor of 0.7025 is applied. The settings used to obtain this result are 10% move-limits and the initial angles from Figure 8.

load factor are an increase in λ_c and a decrease in the b-factor. This is as expected since the design space is smaller, and the previous optimum is infeasible with the imposed buckling load constraint. The Koiter b-factor is decreased by 4%, 12%, and 21% for the three constraints, respectively. Note that the $b\lambda_c$-factor for the case with a constraint of 85% attains a value which is close but lower than when maximizing the $b\lambda_c$-factor. This is an effect of the different optimization formulations, where the constraint on the buckling load factor forces the critical buckling factor always to be feasible. This is not the case when optimizing the $b\lambda_c$-factor, where the buckling load factor can attain any value during the optimization process to reach a different optimum. Regardless, the difference in the post-buckling stability is only 2% between the two optimizations.

The optimum fiber angles for the different optimizations are given in Figures 13-15. Compared to the optimum fiber angles it is seen that the fiber angles for the Max b_{75} case in Figure 13 are similar to those from the unconstrained optimizations. For the two cases with a buckling load constraint of 85% and 90% the center region of the plate is dominated by fibers aligned at approximately 90°. Furthermore, the first column at edge 3 consists of fiber angles which are close to symmetric to those of the last column at edge 1. The right hand side of the panel resembles the fiber angles from the Max b case, see Figure 9, as the fiber angles are aligned in a circular path from the top to the bottom.
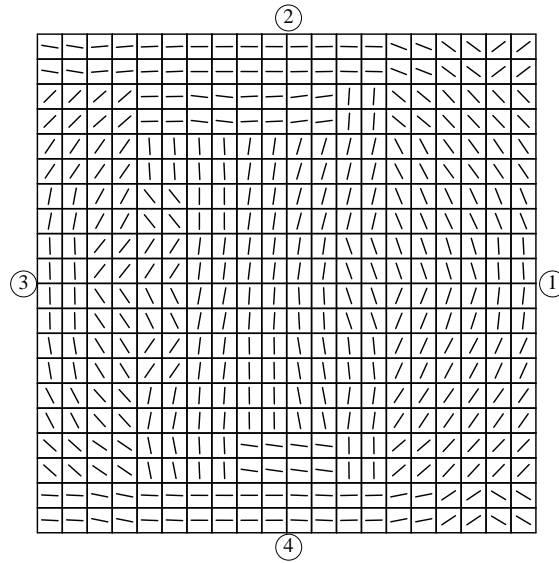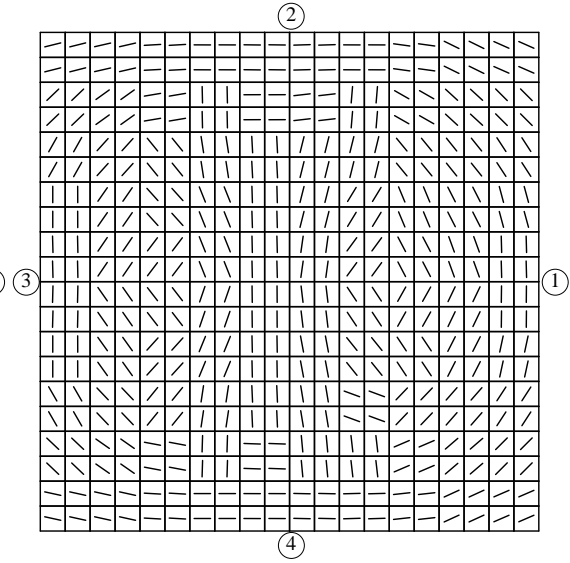
Figure 15. Optimum fiber angles for the Max b_{90} case, with a constraint on the critical buckling load factor of 0.7417. The settings used to obtain this result are 10% move-limits and the initial angles from Figure 8.

6.5. Constraint on the second buckling load factor

Closely distributed eigenvalues are encountered when the buckling load factor for the optimum design is sufficiently close to the maximum attainable buckling load factor. This is not accounted for in the analysis and design sensitivity analysis, as the interaction between the multiple buckling loads is not accounted for. To avoid this, a constraint on the second buckling load factor is imposed, and chosen to be equal to the maximum attainable critical buckling load factor when optimizing the buckling load of the structure. This constraint ensures that multiple buckling loads are not encountered during the optimization. This constraint may result in suboptimal designs compared to optimizing the multiple buckling loads. Regardless, this approach is used, as previously, when multiple eigenvalues can occur during the optimization, see e.g., [40].

Four different cases are shown with this constraint i.e., Koiter b-factor optimization without a constraint on the critical load factor, Max b_2, with a critical buckling load constraint of 85% and 90% of the maximum attainable, Max $b_{85,2}$ and Max $b_{90,2}$, and a $b\lambda_c$-factor optimization, Max $b_2\lambda_c$. The results for the four cases are given in Table VI. As expected, a reduction in the post-buckling factors compared to the unconstrained cases is realized, as the design space is reduced. Comparing the results in Table VI to the results in Table IV and Table V the consequence of the λ_2 constraint is quantified. A decrease of 1% of the b-factor and 8% in λ_c is observed when comparing Max b_2 to the unconstrained Max b case. The fiber angles for the max b optimizations, with and without a constraint on λ_2, are shown in Figure 9 and 16, respectively. The constraint on λ_2 primarily alters the fiber angles at edge 2 and 4 where more patches are aligned at 0° when the constraint is imposed. This explains the low decrease in the b-factor when imposing the constraint. The 85% case exhibits a decrease of 2% in the b-factor compared to the constrained case. The decrease in the b-factor for the 90% case is 1% compared to the constrained case. Lastly, a reduction of 4% in the $b\lambda_c$-factor is seen for the Max $b_2\lambda_c$ case. Based on the results in Tables IV-VI, constraining the higher order buckling loads does not give a significant reduction in the post-buckling response of the structure.

The optimum fiber angles are given in Figures 16-19. Comparing the fiber angles to the plates without constraints on λ_2, Figure 9, Figure 14, Figure 15, and Figure 11, the fiber angles are similar. This result is as expected since the difference in the post-buckling properties is small. The major differences are in the center region where some of the $\pm45°$ patches have switched sign in order to resemble those from the buckling load maximization in Figure 8. Comparing Figure 19 to Figure 11 it is seen that the last three columns of patches are similar between the two, but the remainder of the

Table VI. Optimization results for the square plate with constraint on the second buckling load of 0.8241 defined by the subscript $_2$. The subscript numbers after Max b gives the percent-wise constraint on the critical buckling load factor compared to the maximum attainable, see Table V for the constraint values. The initial angles are given by Figure 8 and move-limits of 10% except for Max b and Max b_{85} where move-limits of 1% provided the best results.

Case	λ_c [-]	λ_2 [-]	b [-]	$b\lambda_c$ [-]
Max b_2	0.5324	0.8241	0.07826	0.04166
Max $b_{85,2}$	0.7025	0.8241	0.06817	0.04789
Max $b_{90,2}$	0.7417	0.8241	0.06151	0.04562
Max $b_2\lambda_c$	0.7164	0.8241	0.06721	0.04815
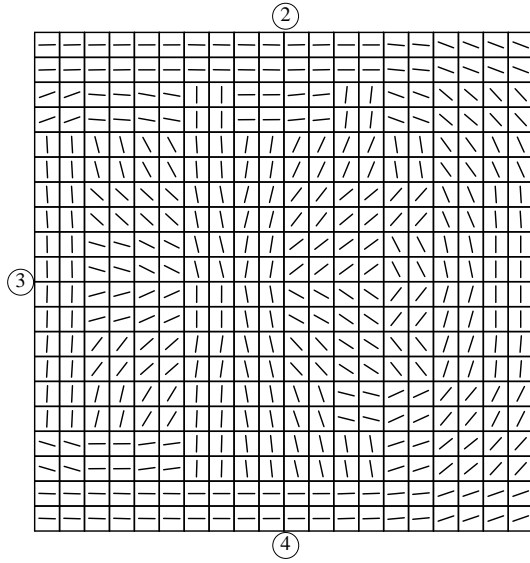
Figure 16. Optimum fiber angles for the Max b_2 case with a constraint on $\lambda_2 = 0.8241$. The settings used to obtain this result are 1% move-limits and the initial angles from Figure 8.

Figure 17. Optimum fiber angles for the Max $b_{85,2}$ case with a constraint on the critical buckling load factor of 0.7025 and $\lambda_2 = 0.8241$ for the single layer square plate. The settings used to obtain this result are 1% move-limits and the initial angles from Figure 8.

structure resembles Figure 14 where the Koiter b-factor is maximized and the critical buckling load is constrained to the buckling load for Max $b\lambda_c$.

6.6. Convergence of the optimizations

In general, three different iteration histories are observed for the plate. The three iteration histories are given in Figures 20-Figure 22. Nearly all optimizations use 200 iterations, and the optimization is terminated due to the convergence limit. This is a consequence of the tight convergence criterion where the normalized change in the design variables must be below 0.00001, which forces the optimization to continue even though only minor changes in the design is observed. The optimization reaches a value close to the optimum b- and $b\lambda_c$-factor within 30 iterations for all cases.

Since all solutions start with the buckling load optimized design, multiple eigenvalues are present in the initial iteration. It is observed that λ_c and λ_2 are separated in the initial iteration for all optimizations. The remaining part of the optimization history depends on the applied constraints. The iteration history for the Max b case is shown in Figure 20. This iteration history shows that λ_c and λ_2 remain separated throughout the evolution of solutions. The drops in the b-factor and kinks for λ_c in the initial 10 iterations are caused by the 10% move limits, as these are not present when tighter move limits are selected. After iteration 20 almost no change in the values is observed which
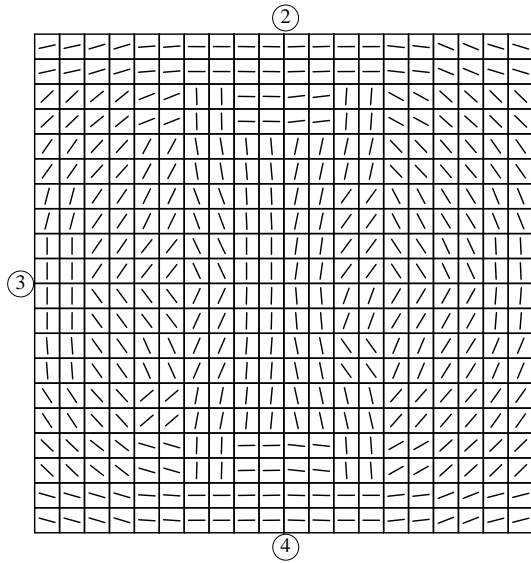
Figure 18. Optimum fiber angles for the Max $b_{90,2}$ case with a constraint on the critical buckling load factor of 0.7417 and $\lambda_2 = 0.8241$ for the plate. The settings used to obtain this result are 10% move-limits and the initial angles from Figure 8.
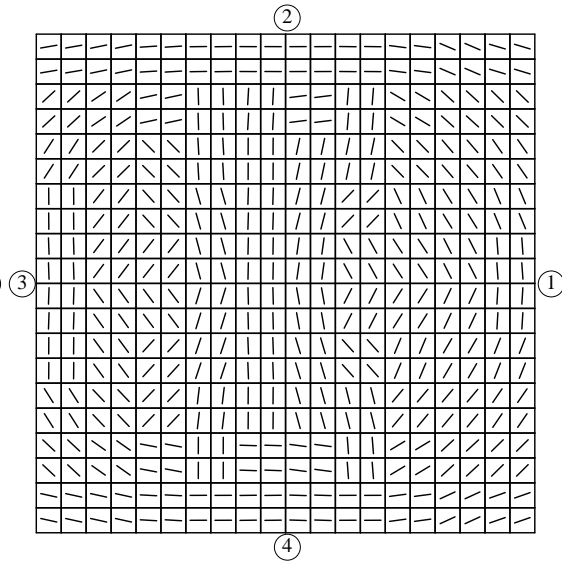
Figure 19. Optimum fiber angles for the Max $b_2\lambda_c$ case. λ_2 is constrained to 0.8241 for the plate. The settings used to obtain this result are 10% move-limits and the initial angles from Figure 8.

supports the conclusion that a tight convergence criterion is selected. Figure 21 gives an iteration history where multiple eigenvalues occur during the optimization, here exemplified with the Max $b\lambda_c$ case. The overall tendencies are the same as Figure 20 except for the drops in the b-factor. These drops are caused by the multiple eigenvalues, where the two lowest eigenvalues switch position, and the lower b-factor for the second eigenvalue enters the objective function. This consideration further demonstrates the need for constraining the second eigenvalue to avoid this switching. To test whether the optimized post-buckling response from the second buckling load leads to a different optimum, optimizations where the second buckling load is the lowest have been performed. The Max b, Max $b\lambda_c$, and Max b with a constraint on the original λ_c have been performed. The optimizations converge to the results with λ_c as the lowest. The last iteration history, Figure 22, is the Max $b_{90,2}$ case which displays a case where the second buckling load factor is constrained. This iteration history resembles that from the Max b case with the difference being that the second buckling load factor does not decrease in the initial iteration. For the cases with a constraint on λ_2 convergence is observed prior to the iteration limit.

6.7. *Comparison of post-buckling response*

In this section we compare the post-buckling response of some of the cases shown in the previous sections. Two plots are used to compare the post-buckling responses, first the change in load factor, λ, as a function of the expansion parameter, ξ, and the load-end shortening responses. The $\xi - \lambda$ plots are given in Figure 23. This figure displays the interaction between the critical buckling load factor and the post-buckling stability, as the curves for the buckling load maximized structure and the post-buckling optimized structures cross in the post-buckling regime. The proposed methods successfully provide structures which are more stable in the post-buckling region compared to the $0°$ case and the buckling load maximized structure, Max λ_c, because of the larger post-buckling curvature. Furthermore, optimized designs with similar critical load factor display similar post-buckling behavior regardless of the chosen buckling formulation. The importance of a constraint on the buckling load when maximizing the b-factor can be seen in the figure, since a low buckling load causes the perturbation to be far into the post-buckling regime before it crosses a curve with a
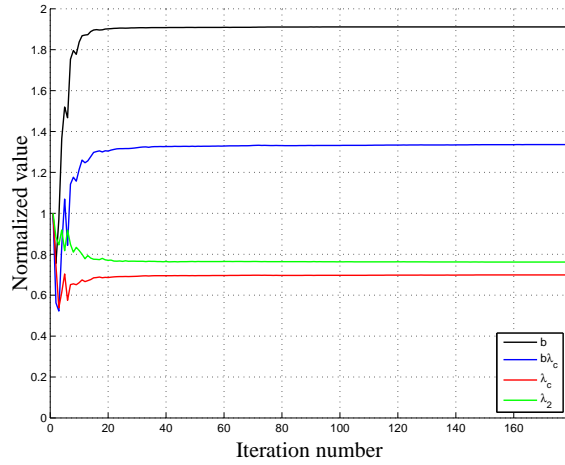
Figure 20. Optimization history for the Max b case in Table IV. The normalization factors used are the initial values, i.e., the results from the Max λ_c case in Table IV. The initial decrease in the post-buckling factors is a consequence of the multiple eigenvalues.
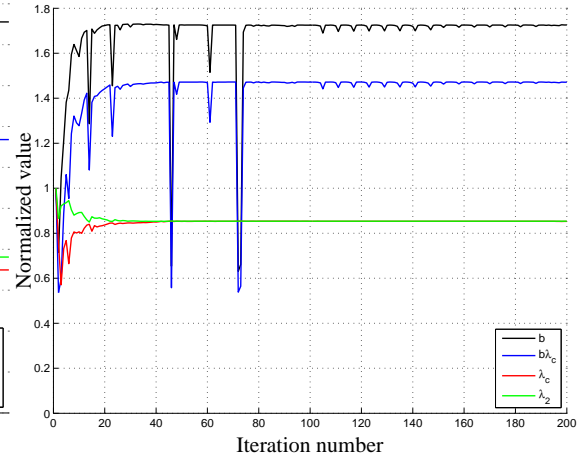

Figure 21. Optimization history for the Max $b\lambda_c$ case in Table IV. The normalization factors used are the initial values, i.e., the results from the Max λ_c case in Table IV. The initial decrease in the post-buckling factors is a consequence of the multiple eigenvalues. The drops at the later iterations are caused by the second eigenvalue.
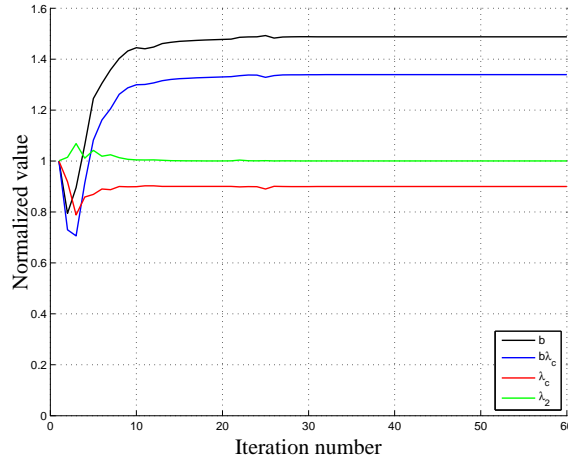
Figure 22. Optimization history for the Max $b_{90,2}$ case in Table VI. The initial b and $b\lambda_c$ values are used to normalize the corresponding curves. The critical buckling load factor is used to normalize λ_c and λ_2. Convergence of the optimization is observed after 58 iterations.

larger buckling load. Since the $b\lambda_c$-factor is used when determining the post-buckling load factor, the unconstrained $b\lambda_c$ case displays the largest load factor in the far post-buckling field.

The load-end shortening curves for the cases are shown in Figure 24. The curves are obtained by inserting the displacement fields, critical buckling load, and Koiter b-factor into Equation (5). This plot reveals the drop in the inplane stiffness in the post-buckling regime. The 0° case displays the highest resistance towards end shortening both at a pre- and post-buckling configuration, this is as expected, as all the fibers are aligned in the loading direction. For the optimized structures the pre-buckling stiffness decreases because the fiber angles are changed from 0° and thus the stiffness towards the load decreases. The relative decrease in stiffness between the pre- and post-buckling response is lower for the post-buckling optimized structures compared to the 0° and buckling load optimized structures. For example, the stiffness drop for the Max b case is small, and at an end
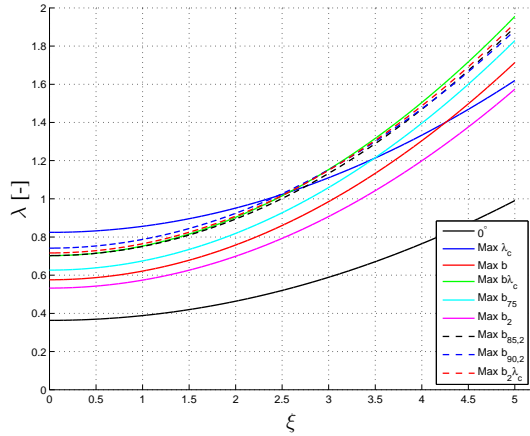
Figure 23. Post-buckling response for selected cases, see Tables III-VI for legend meanings. Note that neither the interaction between the different buckling modes are taken into account nor possible mode switching in the post-buckling configuration.
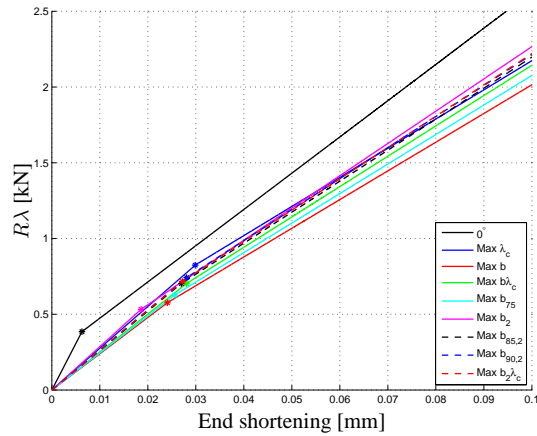
Figure 24. Load-end shortening response for selected cases, see Tables III-VI for legend meanings. The asterisk on each line gives the buckling point. The stiffness decreases in the post-buckling region for all optimizations.

shortening of 0.1 ($4\times$ the buckling end shortening) the difference in load factor for the buckled configuration and an extrapolation of the pre-buckling response is approximately 20%.

6.8. Comparison to geometrically non-linear analysis

To demonstrate the validity of the post-buckling analysis and optimization, the results are compared to geometrically non-linear (GNL) finite element analyses. The GNL analyses are performed using the approaches from [41] and branching to the secondary equilibrium curve is performed by assigning a small imperfection in the plate. For nearly all cases good correlation between the analyses is observed. Figure 25 and Figure 26 display the post-buckling responses for the Max $b\lambda_c$ and Max b cases. For the Max $b\lambda_c$ case the out-of-plane displacement is accurately captured by the Koiter analysis. The kink at a load factor of approximately 1.55 [kN] arises from mode switching in the non-linear analysis. In the Max b case, Figure 26, mode switching occurs at a load factor of 0.6 [kN]. This is not captured by the Koiter analysis, which is evident in the end shortening response of the plate, where the softening caused by mode switching is not present in the Koiter analysis. Mode switching is not included into the perturbation, and thus cannot be captured by the asymptotic analysis, see Equation (4). When mode switching occurs in the analysis, it is important to evaluate whether the load is above the design load. If mode switching occurs within the operational area, a multi mode Koiter analysis should be applied [20].

Comparing the responses in Figure 25 and Figure 26 to the response for the 0° case in Figure 3 the importance of selecting the correct post-buckling criteria is realized. As demonstrated in Figure 24 the 0° case provides the best stiffness against the end shortening, but the out-of-plane displacements are larger for the 0° case compared to the Max b and Max $b\lambda_c$ cases. Also a simple minimization of the maximum out-of-plane displacement may not directly work on the buckling phenomena causing the large displacement, as the buckling problem is not directly included into the optimization problem.

7. CURVED PANEL

The second example is the curved panel given in Figure 27. All edges are restrained from displacement in the x-direction. The load is applied as a displacement in z at one of the curved edges and the other is restrained in the z-direction. All edges are free to rotate. The two center nodes on the curved edges are constrained in the y-direction to create a definite system matrix. The
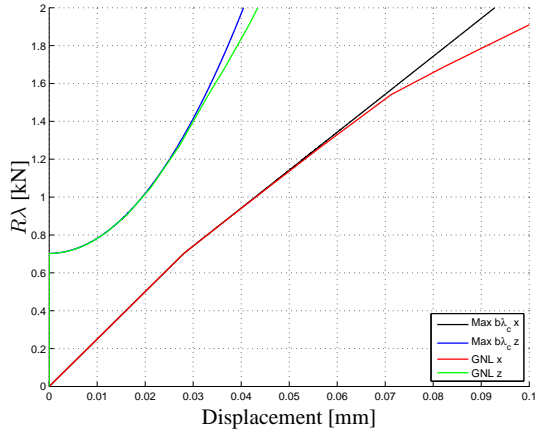
Figure 25. Comparison between the Max $b\lambda_c$ case and geometrically non-linear analysis, GNL. Displacement refers to either the end shortening, Max $b\lambda_c$ x and GNL x, or 1/100 of the normal deflection for the center node in the buckle, Max $b\lambda_c$ z and GNL z. The kink at a load factor of 1.55 [kN] is caused by mode switching.
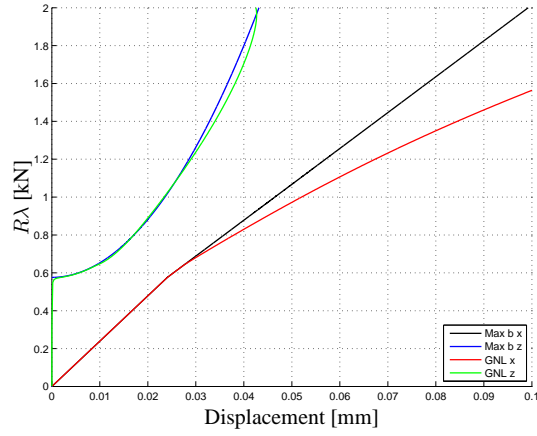
Figure 26. Comparison between the Max b case and geometrically non-linear analysis, GNL. Displacement refers to either the end shortening, Max b x and GNL x, or 1/100 of the normal deflection for the center node in the buckle, Max b z and GNL z. At a load factor of 0.6 [kN] branch switching occur. This explains the deviation of inplane displacements between the Koiter and GNL analyses.
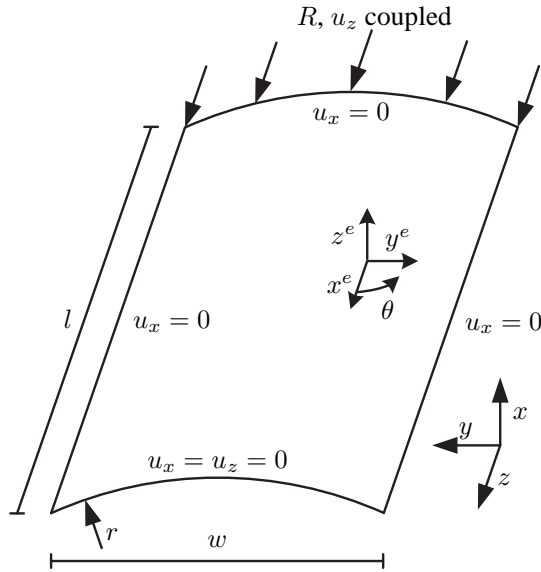

Figure 27. Load and supports for the panel. Coupled defines that the nodes along the edge are forced to have the same z-displacement. The load R is applied as a displacement along the edge. The $x^e y^e z^e$-coordinate system defines the element coordinate system.

dimensions of the panel are given in Table VII, and the material properties are the same as for the plate, see Table II. 400 quadratic shell elements provide a converged discretization for the Koiter analysis, and they are grouped into one patch. The panel consists of 8 layers of equal thickness, and the orientations of each layer are used as design variables.

The curved panel displays an example which exhibits asymmetric buckling. From this we aim to show how to design structures which exhibits asymmetric ($a \neq 0$) buckling. Additionally, this example demonstrates the applicability of the proposed methods and the limitations of the Koiter analysis.

Table VII. Dimensions and load for the curved panel.

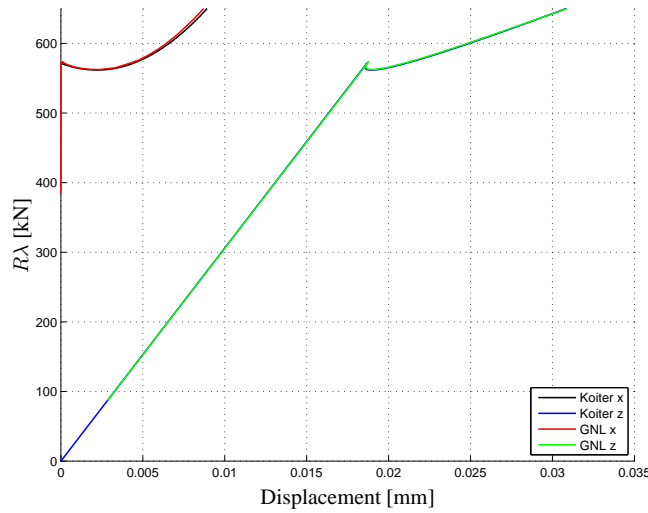| Parameter	Unit	
Side length, l	[mm]	100
Width, w	[mm]	100
Radius, r	[mm]	1000
Thickness, t	[mm]	1
Load, R	[kN]	1.0

Figure 28. Comparison between the Max b case and geometrically non-linear analysis, GNL, for the curved panel. Displacement refers to either the end shortening, Koiter z and GNL z, or -1/100 of the normal deflection for the center node, Koiter x and GNL x.

7.1. Analysis of the panel

To demonstrate the behavior of the panel all fiber angles are chosen to be $0°$. The post-buckling responses are given in Figure 28 for the Koiter analysis and GNL finite element analysis, respectively. The pre-buckling response from the GNL finite element analysis is linear. Buckling is predicted at 572 [kN]. This buckling load is distinct since the second buckling load is 1270 [kN]. The post-buckling response from Koiter analysis is asymmetric with an inwards buckle resulting in a decrease in the load. The stability is recovered at a load of 562 [kN]. The asymmetry in the post-buckling response arises from the curvature of the panel. Development of the buckle in the positive x-direction is affine with a stretching of the membrane and thus the behavior is similar to a flat plate which exhibits a stable post-buckling response. The same post-buckling behavior is observed for the GNL finite element analysis, and the Koiter analysis correctly captures the snap-through and the following post-buckling response.

7.2. Optimization of the panel

During the optimization, the panel displayed a low sensitivity towards the settings of the optimizer. Move limits of 1% are used for all examples, and the same convergence criterion as for the plate has been applied, i.e., $\sqrt{\dfrac{\sum_{i=1}^{n^e} \Delta\theta_i^2}{\sum_{i=1}^{n^e} \left(\overline{\theta}_i - \underline{\theta}_i\right)^2}} < 0.00001$. The optimum design for the b-factor without any constraints on the critical buckling load factor or a-factor is to have all layers oriented at $0°$. The $0°$ case represents one of the two baseline designs. The second baseline design is the buckling load maximized panel.

The results from the optimization are given in Table VIII. During the maximization of the critical buckling load factor no multiple eigenvalues are observed. The first and second buckling load factors

Table VIII. Results for the optimization of the curved panel. Case defines the optimization problem considered. $0°$ represents the baseline design where the b-factor is maximized. Max λ_c^r are the rounded fiber angles from the optimum buckling load design. The subscript after $|a|$ defines the buckling load constraint whereas a superscript is the b-factor constraint. The superscript after Max b defines the constraint on the a-factor. The second column contains the critical buckling load factors. The third and fourth columns are the Koiter a and b-factors. The last columns are the orientations for each ply in the laminate.

Case	λ_c [-]	a 10^{-2} [-]	b 10^{-2} [-]	Layup 1	2	3	4	5	6	7	8
$0°$ (Max b)	571.6	3.146	1.434	0.0	0.0	0.0	0.0	0.0	0.0	0.0	0.0
Max λ_c	785.0	3.431	0.244	-46.3	-47.0	46.0	57.8	92.9	92.2	44.9	-42.6
Max λ_c^r	784.1	3.369	0.243	-45.0	-45.0	45.0	60.0	90.0	90.0	45.0	-45.0
Min $|a|$	599.0	1.701	0.843	1.5	0.0	-1.5	-6.0	37.5	46.6	50.6	-51.8
Min $|a|_{650}$	650.0	1.881	0.681	-14.8	16.8	6.9	-19.8	-37.3	-45.9	48.6	-52.4
Min $|a|_{700}$	700.0	2.054	0.547	-25.1	24.2	10.8	-22.6	-38.4	-46.9	49.5	-53.0
Min $|a|_{750}$	750.0	2.635	0.298	-40.0	-35.0	39.9	32.1	43.6	-52.8	51.9	-53.4
Min $|a|^1$	559.3	1.822	1.0	-0.7	0.7	1.8	2.8	11.9	44.6	49.8	52.4
Min $|a|^{1.1}$	562.3	1.955	1.1	-1.1	-0.5	0.1	0.5	0.3	25.9	45.6	49.9
Min $|a|^{1.2}$	572.2	2.176	1.2	-1.2	-0.9	-0.5	-0.1	0.3	0.6	34.5	46.1
Min $|a|^{1.3}$	581.5	2.535	1.3	-0.9	-0.8	-0.6	-0.4	-0.1	0.6	4.3	38.8
Max $b^{1.75}$	595.7	1.75	0.953	0.6	-0.2	-1.1	-2.6	11.9	44.5	49.5	-51.5
Max $b^{1.85}$	598.0	1.85	1.041	-0.3	-0.6	-0.9	-1.4	-2.5	27.1	45.8	-49.4
Max b^2	599.5	2.0	1.126	0.0	-0.2	-0.4	-0.7	-1.0	-2.8	41.9	-48.8
Max $b^{2.1}$	598.7	2.1	1.163	-0.2	-0.3	-0.5	-0.8	-1.3	-2.6	32.5	-46.3
Max $b^{2.2}$	596.9	2.2	1.196	-0.1	-0.3	-0.6	-0.9	-1.4	-3.0	25.4	-45.2
Max $b^{2.5}$	581.2	2.5	1.291	0.9	0.8	0.6	0.3	0.0	-0.6	-6.1	-41.3

are separated by 24% in the optimized design. As expected, the majority of the layers are aligned at approximately $\pm45°$. Two layers are aligned at $90°$. Rounding the fiber angles as shown in the table provides a negligible decrease in the buckling load of 0.1% and thus the slightly off-angled design provides a better design compared to the rounded design. Compared to the $0°$ design the buckling load is increased by 37% whereas the b-factor is decreased by 83% and the a-factor is increased by 8%. Consequently, the buckling load is increased but the post-buckling performance is decreased.

7.3. Optimization of the asymmetric response

The panel exhibits asymmetric buckling, and thus the initial post-buckling response is unstable. The asymmetry is caused by the non-zero a-factor, and in order to obtain a more symmetric response the a-factor should be as close to zero as possible. The optimization problem solved is described by Equations (60)-(64), and we will demonstrate the effect of constraining both the b-factor and the critical buckling load, all results are presented in Table VIII.

Minimizing the absolute a-factor without constraints on the b-factor nor the critical buckling load factor is performed to demonstrate the capabilities when minimizing the asymmetry in the post-buckling response, Min $|a|$ in Table VIII. Figure 29 displays the normal component of the pre-buckling displacement field $^0\mathbf{U}$. The normal displacements eliminate the initial curvature of the panel by utilizing the bending-extension couplings in the laminate. This can be seen in the layup, which consists of plies aligned at approximately $0°$ for the first four layers and at approximately $\pm45°$ for the remaining layers. The pre-buckling displacements flatten the panel, and thus pushes the buckling response towards the symmetric buckling of a flat plate. The buckling load is increased by 5% compared to the $0°$ case, and the b-factor is decreased by 41%. However, the a-factor is decreased by 46% and thus a more symmetric response is obtained.

The critical buckling load factor is 31% lower for the $|a|$ optimized panel than for the buckling load maximized panel. Hence a constraint on λ_c can be applied to increase the buckling load. The effect of this constraint is demonstrated in the following. Three constraints on the critical buckling load factor are used, and the constraint is assigned a value of $\underline{\lambda_1} = \{650, 700, 750\}$. The optimum
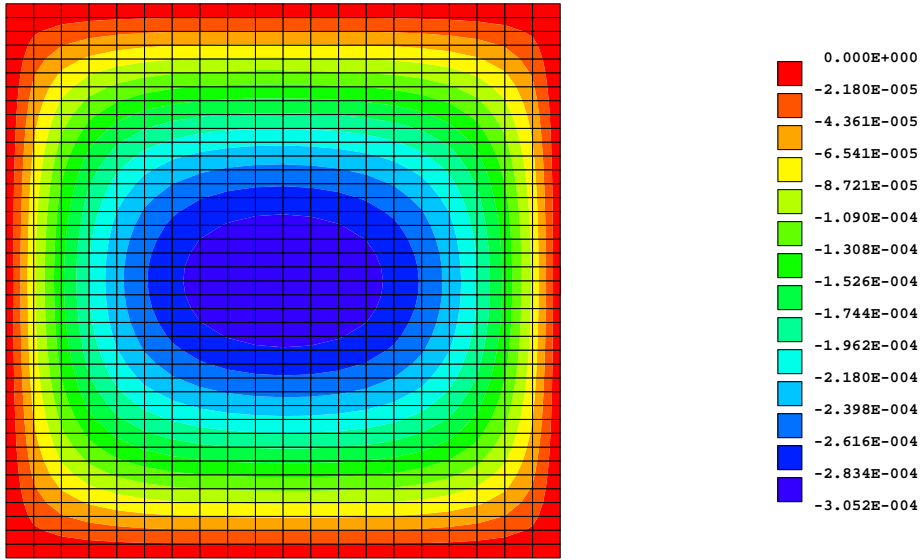
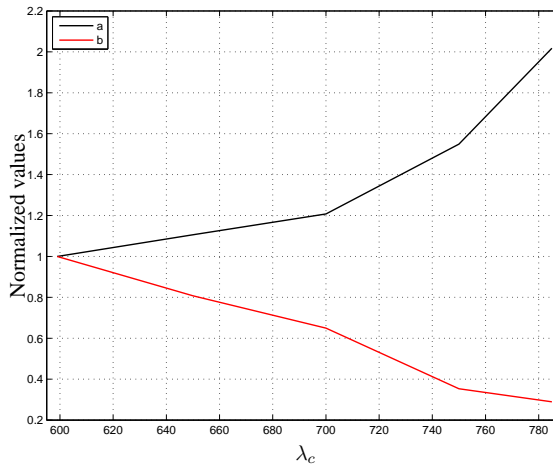Figure 29. X-component of the ^{0}U displacement field for the Min $|a|$ case. The load is applied on the right edge.

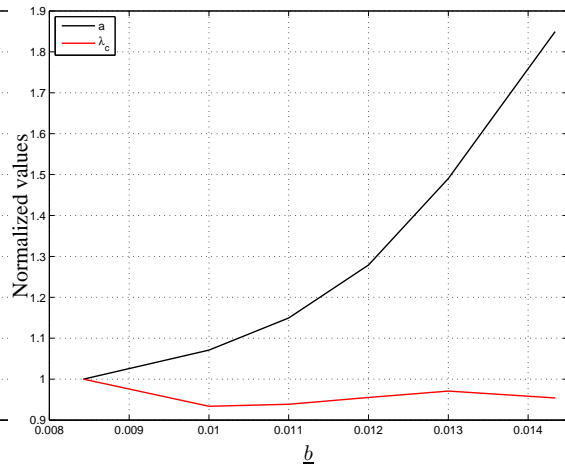Figure 30. Dependence of the λ_1 constraint on the a and b-factors for the curved panel.

Figure 31. Dependence of the $\underline{b}$ constraint on the a-factor and the critical buckling load for the curved panel.

fiber angles from the buckling load optimization are used as initial angles to ensure a feasible design in the first iteration. The results are given in Table VIII. Figure 30 presents the a and b-factors for the optimized designs as a function of the critical buckling load constraint. As expected, the a-factor increases and the b-factor decreases as the critical buckling load increases towards the maximum attainable. This is a consequence of the design being pushed towards the buckling load optimized design in order to comply with the constraint on the buckling load, and thus the a and b-factors approaches those from the buckling load optimized case.

The b-factor is reduced by 41% for the $|a|$ optimized case compared to the $0°$ case. Constraining the b-factor allows the curvature of the load factor to attain a certain minimum value. The minimum bound on the b-factor is in this case of $\{0.01, 0.011, 0.012, 0.013\}$ to demonstrate the effect on the optimum a-factor. The optimizations are initialized with all design variables aligned at $0°$ which provides a feasible design in the initial iteration. The optimum designs are given in Table VIII and in Figure 31. The a-factor increases as the constraint on the b-factor approaches that for the $0°$ design.
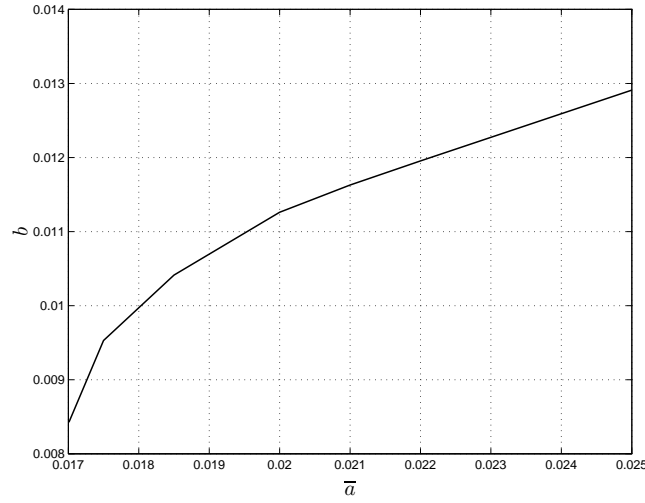
Figure 32. Dependence of the $\overline{a}$ constraint on the b-factor for the curved panel.

This is as expected since more layers must be aligned close to $0°$ in order to satisfy the constraint. The buckling load factor remains almost constant for the different constraint values. Due to the fact that the buckling loads for the a and b-factor optimizations are close.

7.4. Optimization of the b-factor

Even though the initial post-buckling response is unstable, optimization of the b-factor can still be important. Maximizing the b-factor ensure the structure is as stable as possible when the $b\lambda_c\xi^2$-term becomes dominant in the load factor expansion, see Equation (4). Only a-factor constrained optimization is shown as the optimum design for the unconstrained case has been described, and the effect of constraining the critical load factor behaves as in the previous example. Constraint values of $\overline{a} = \{0.0175, 0.0185, 0.02, 0.021, 0.022, 0.025\}$ are chosen. The results for the different selections of the constraint values are given in Table VIII with the initial angles being the ones for the Min $|a|$ case. As expected, when imposing constraints to have a more symmetric post-buckling response the value for the b-factor decreases. The correlation between the $\overline{a}$ constraint and the b-factors is given in Figure 32. As the constraint on $\overline{a}$ is increased i.e., more asymmetry is allowed, the b-factor increases in a logarithmic manner. The critical buckling load factor remains almost constant throughout the optimization as the buckling loads for the Max b and Min $|a|$ cases are similar. As the constraint on the a-factor increases the fiber angles approaches $0°$ which is expected since the design space becomes larger. The layer orientations approach $0°$ from the first layer to the eighth layer as the constraint is increased. Because of the geometry, the outer layers give the largest contribution to the membrane-bending coupling which minimizes the a-factor.

From these studies, we observe that the Koiter a-factor behaves in a similar manner as the b-factor when constraints are applied to the optimization.

7.5. Comparison of post-buckling response

The post-buckling responses predicted by Koiter analysis for the $0°$ (Max b), Min $|a|$, and Max λ_c cases are given in Figure 33 and Figure 34 for the center node and end shortening, respectively. Furthermore, the geometrically non-linear responses for the Min $|a|$ and Max λ_c cases are also presented in the figures. Focus is initially given to the asymptotic responses, and afterwards the geometrically non-linear responses.

The asymptotic responses display the expected behavior for the different optimizations. The Max λ_c case has the highest buckling load factor, but loses the stiffness in the post-buckling regime. The load factor drops to a value of 690 [kN] before stability is regained. Note that for the asymptotic
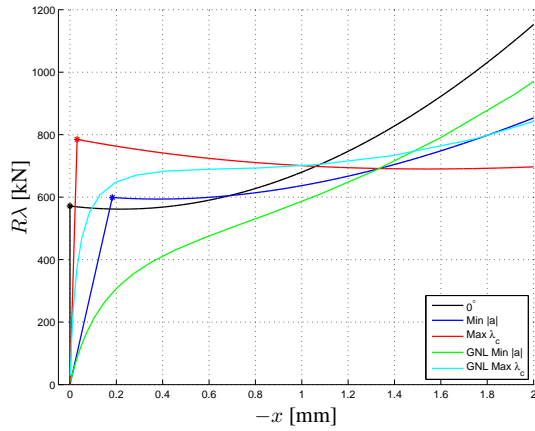
Figure 33. Negative out-of-plane displacement for the center node. $0°$, Min $|a|$, and Max λ_c refer to Koiter analysis. GNL Min $|a|$ and GNL Max λ_c are the geometrically non-linear analyses with the layup from Min $|a|$ and Max λ_c, respectively. Recall that the GNL analysis and Koiter analysis for the $0°$ case are coincident, and thus the GNL case is not given in the figure.

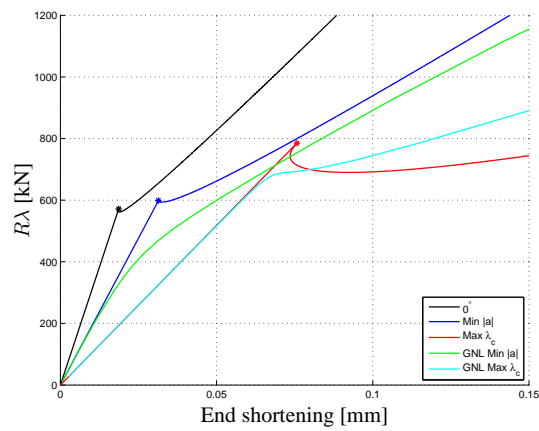Figure 34. Load-end shortening response for the panel. $0°$, Min $|a|$, and Max λ_c refer to Koiter analysis. GNL Min $|a|$ and GNL Max λ_c are the geometrically non-linear analyses with the layup from Min $|a|$ and Max λ_c, respectively. Recall that the GNL analysis and Koiter analysis for the $0°$ case are coincident, and thus the GNL case is not given in the figure.

responses, the load factors for the $0°$ and Min $|a|$ cases are 33.8% and 8.4% higher at the out-of-plane displacement where the Max λ_c case regains stability, 1.6 [mm], respectively. The Min $|a|$ case displays almost no decrease in the load when buckling occur, thus shows that the proposed method successfully minimizes the asymmetry in the buckling response, and that the decrease in load can be minimized by optimizing the a-factor. The $0°$ case reveals that optimizing the Koiter b-factor still makes sense even though the initial post-buckling response is unstable, as the structure regains the stability at a lower displacement, and that the out-of-plane displacements efficiently are minimized.

When considering the geometrically non-linear response, recall from Figure 28 that the Koiter analysis produced an accurate approximation of the geometrically non-linear response for the $0°$ case. For the Min $|a|$ and Max λ_c cases only the initial part of the pre-buckling response for the out-of-plane displacements in Figure 33 is accurately captured by the Koiter analysis. The end shortening also deviates for the two analyses in the pre-buckling response. The reason for the divergence between the two analyses is that the membrane-bending coupling acts as an imperfection for the bifurcation buckling when out-of-plane displacements arise which cannot be captured by the linear buckling analysis. Both geometrically non-linear analyses reveal that the panel remains stable throughout the analysis, and thus the snap-through predicted by the Koiter analysis is not present in the geometrically non-linear response. Regardless, the optimized structures reveal some of the same properties in the non-linear cases: the Min $|a|$ case possesses more stiffness as the non-linearities becomes more significant, whereas increasing the load factor from 650 to 700 for the buckling load optimized case provides an increase in the out-of-plane displacements of 400%. In conclusion, Koiter analysis and design optimization successfully enable the possibility of optimizing the post-buckling response of the panel even though pre-buckling nonlinearities are present. If the linear buckling analysis does not provide a good estimate of the buckling load and mode shape, it is important to switch to non-linear buckling analysis. Furthermore, we observe that even though the analysis is not completely accurate the design sensitivities still provide the information needed to optimize the post-buckling response.

8. CONCLUSION

This work presents a novel method for post-buckling design optimization of laminated composite structures. The proposed method is based on Koiter's asymptotic method for post-buckling analysis. The design sensitivities of the Koiter factors are derived. To demonstrate the use of Koiter's method for optimum design two different objective functions based on the b-factor and one based on the a-factor are shown and compared. The objective functions are used to limit development of the post-buckling shape or to minimize the asymmetry in the post-buckling response. Minimization of the development of the post-buckling shape is important if a shape close to the initial unbuckled shape is required, while the structure is operated in a post-buckling configuration. This approach also minimizes the risk of failure of laminates due to high strain levels in a post-buckling configuration. Minimization of the asymmetry is important to minimize the decrease in load factor for the initial post-buckling response.

For validation purposes, our approach is compared to analytical and geometrical non-linear (GNL) analysis. From this, post-buckling optimization is carried out on a square plate and a curved panel to demonstrate the capabilities of the proposed methods. The two examples where the fiber angles for a fixed thickness are optimized demonstrates the possibility of optimizing the post-buckling response for both a symmetric and asymmetric point of bifurcation. These examples show the effect of constraining either the critical load factor, λ_c, and the Koiter a and b-factors. The effect of the constraints can be explained by considering maximization of the b-factor while constraining the critical load factor. If no constraint on the load factor is present, the b-factor is maximized. Increasing the load factor constraint towards that of the maximum buckling load causes a decrease of the b-factor until that of the buckling load maximized case is reached. The same effect is observed when applying the different combinations of objectives and constraints with respect to λ_c, a, and b.

The importance of applying the correct post-buckling optimization criterion is also revealed in this work. Considering the out-of-plane displacements and end shortening for plates and curved panels we show that the optimum laminate configurations for minimizing the two displacements are different. This result is important as it requires the engineer to determine which of the two responses is critical for the structure before conducting any post-buckling optimization.

The presented design sensitivity analysis is derived in a general sense, hence can be applied to other parametrizations including layer thicknesses, Discrete Material Optimization, lamination parameters etc.

REFERENCES

1. Thompson J. Optimization as a generator of structural instability. *International Journal of Mechanical Sciences* 1972; **14**(9):627–629.
2. Lindgaard E, Lund E, Rasmussen K. Nonlinear buckling optimization of composite structures considering "worst" shape imperfections. *International Journal of Solids and Structures* 2010; **47**(22-23):3186–3202.
3. Henrichsen SR, Lindgaard E, Lund E. Robust buckling optimization of laminated composite structures using discrete material optimization considering worst shape imperfections. *Thin-Walled Structures* 2015; **94**(0):624 – 635.
4. Yao W, Chen X, Luo W, van Tooren M, Guo J. Review of uncertainty-based multidisciplinary design optimization methods for aerospace vehicles. *Progress in Aerospace Sciences* 2011; **47**(6):450 – 479.
5. Bažant Z, Cedolin L. *Stability of Structures: Elastic, Inelastic, Fracture and Damage Theories*. World Scientific, 2010.
6. Arbocz J, Starnes J Jr. Future directions and challenges in shell stability analysis. *Thin-Walled Structures* 2002; **40**(9):729–754.
7. Zimmermann R, Klein H, Kling A. Buckling and postbuckling of stringer stiffened fibre composite curved panels - tests and computations. *Composite Structures* 2006; **73**(2):150 – 161. International Conference on Buckling and Postbuckling Behavior of Composite Laminated Shell Structures.

8. Degenhardt R, Castro SG, Arbelo MA, Zimmerman R, Khakimova R, Kling A. Future structural stability design for composite space and airframe structures. *Thin-Walled Structures* 2014; **81**:29–38.

9. Riks E. An incremental approach to the solution of snapping and buckling problems. *International Journal of Solids and Structures* 1979; **15**(7):529–551.

10. Crisfield M. A fast incremental/iterative solution procedure that handles "snap-through". *Computers & Structures* 1981; **13**(1-3):55–62.

11. Bender CM, Orszag SA. *Advanced Mathematical Methods for Scientists and Engineers*. McGraw-Hill, 1978.

12. Koiter WT. The stability of elastic equilibrium. PhD Thesis, Technische Hooge School Delft 1945. Translated by E. Riks.

13. Budiansky B. Theory of buckling and post-buckling behavior of elastic structures. *Advances in Applied Mechanics* 1974; **14**:1–65.

14. Byskov E, Hutchinson W. Mode interaction in axially stiffened cylindrical shells. *AIAA Journal* 1977; **15**(7):941–948.

15. Byskov E, Christensen CD, Jørgensen K. Elastic postbuckling with nonlinear constraints. *International Journal of Solids and Structures* 1996; **33**(17):2417–2436.

16. Olesen JF, Byskov E. Accurate determination of asymptotic postbuckling stresses by the finite element method. *Computers & Structures* 1982; **15**(2):157–163.

17. Arbocz J, Hol J. Koiter's stability theory in a computer-aided engineering (CAE) environment. *International Journal of Solids and Structures* 1990; **26**(910):945–973.

18. Lanzo AD, Garcea G. Koiter's analysis of thin-walled structures by a finite element approach. *International Journal for Numerical Methods in Engineering* 1996; **39**(17):3007–3031.

19. Garcea G, Madeo A, Zagari G, Casciaro R. Asymptotic post-buckling FEM analysis using corotational formulation. *International Journal of Solids and Structures* 2009; **46**(2):377–397.

20. Rahman T, Jansen E. Finite element based coupled mode initial post-buckling analysis of a composite cylindrical shell. *Thin-Walled Structures* 2010; **48**(1):25–32.

21. White S, Raju G, Weaver P. Initial post-buckling of variable-stiffness curved panels. *Journal of the Mechanics and Physics of Solids* 2014; **71**(0):132–155.

22. Cochelin B, Damil N, Potier-Ferry M. Asymptotic-numerical methods and Pade approximants for non-linear elastic structures. *International Journal for Numerical Methods in Engineering* 1994; **37**(7):1187–1213.

23. Vannucci P, Cochelin B, Damil N, Potier-Ferry M. An asymptotic-numerical method to compute bifurcating branches. *International Journal for Numerical Methods in Engineering* 1998; **41**(8):1365–1389.

24. Bushnell D. Optimization of composite, stiffened, imperfect panels under combined loads for service in the postbuckling regime. *Computer Methods in Applied Mechanics and Engineering* 1993; **103**(1-2):43–114.

25. Raju G, White S, Wu Z, Weaver PM. Optimal Postbuckling Design of Variable Angle Tow Composites using Lamination Parameters. *Proceedings of 56th AIAA/ASCE/AHS/ASC Structures, Structural Dynamics, and Materials Conference*, American Institute of Aeronautics and Astronautics, 2015.

26. White S, Weaver P. Towards Imperfection Insensitive Buckling Response of Shell Structures-Shells with Plate-like Post-buckled Responses. *Aeronautical Journal* 2015; :1–15Accepted for publication July 2015.

27. Diaconu CG, Weaver PM. Approximate Solution and Optimum Design of Compression-Loaded, Postbuckled Laminated Composite Plates. *AIAA Journal* 2005; **43**(4):906–914.

28. Diaconu CG, Weaver PM. Postbuckling of long unsymmetrically laminated composite plates under axial compression. *International Journal of Solids and Structures* 2006; **43**(2223):6978–6997.

29. Lindgaard E, Dahl J. On compliance and buckling objective functions in topology optimization of snap-through problems. *Structural and Multidisciplinary Optimization* 2013; **47**(3):409–421.

30. Overgaard L, Lund E, Thomsen O. Structural collapse of a wind turbine blade. part a: Static test and equivalent single layered models. *Composites Part A: Applied Science and Manufacturing* 2010; **41**(2):257 – 270.

31. Byskov E. *Elementary Continuum Mechanics for Everyone*. 1st edn., Springer-Verlag, Berlin, 2013.

32. Lund E. Buckling topology optimization of laminated multi-material composite shell structures. *Composite Structures* 2009; **91**(2):158–167.

33. Lindgaard E, Lund E. Nonlinear buckling optimization of composite structures. *Computer Methods in Applied Mechanics and Engineering* 2010; **199**(37-40):2319–2330.

34. Nelson RB. Simplified calculation of eigenvector derivatives. *AIAA journal* 1976; **14**(9):1201–1205.

35. Bendsøe MP, Olhoff N, Taylor JE. A variational formulation for multicriteria structural optimization*. *Journal of Structural Mechanics* 1983; **11**(4):523–544.

36. Olhoff N. Multicriterion structural optimization via bound formulation and mathematical programming. *Structural optimization* 1989; **1**(1):11–17.

37. Svanberg K. The method of moving asymptotes-a new method for structural optimization. *International Journal for Numerical Methods in Engineering* 1987; **24**(2):359–373.

38. MUST. The MUltidisciplinary Synthesis Tool 2015. URL http://www.must.m-tech.aau.dk/, Department of Mechanical and Manufacturing Engineering, Aalborg University.

39. Chandra R, Raju B. Postbuckling analysis of rectangular orthotropic plates. *International Journal of Mechanical Sciences* 1973; **15**(1):81–97.

40. Bendsøe M, Sigmund O. *Topology Optimization: Theory, Methods and Applications*. 2nd edn., Springer-Verlag, Berlin, 2003.

41. Lindgaard E, Lund E. A unified approach to nonlinear buckling optimization of composite structures. *Computers & Structures* 2011; **89**(3-4):357–370.